Monthly Notices
of the
ROYAL ASTRONOMICAL SOCIETY

Mon. Not. R. Astron. Soc. **400,** 1785–1802 (2009) doi:10.1111/j.1365-2966.2009.15625.x

Very light magnetized jets on large scales – I. Evolution and magnetic fields

V. Gaibler,[1⋆] M. Krause[2,3] and M. Camenzind[1]

[1]*Landessternwarte, Zentrum für Astronomie, Universität Heidelberg, Königstuhl 12, 69117 Heidelberg, Germany*
[2]*Max-Planck-Institut für extraterrestrische Physik, Giessenbachstraße 1, 85748 Garching, Germany*
[3]*Universitäts-Sternwarte, Ludwig-Maximilians-Universität (USM), Scheinerstr. 1, 81679 München, Germany*

Accepted 2009 August 26. Received 2009 August 12; in original form 2009 February 6

ABSTRACT

Magnetic fields, which are undoubtedly present in extragalactic jets and responsible for the observed synchrotron radiation, can affect the morphology and dynamics of the jets and their interaction with the ambient cluster medium. We examine the jet propagation, morphology and magnetic field structure for a wide range of density contrasts, using a globally consistent setup for both the jet interaction and the magnetic field. The magnetohydrodynamic code NIRVANA is used to evolve the simulation, using the constrained transport method. The density contrasts are varied between $\eta = 10^{-1}$ and 10^{-4} with constant sonic Mach number 6. The jets are supermagnetosonic and simulated bipolarly due to the low jet densities and their strong backflows. The helical magnetic field is largely confined to the jet, leaving the ambient medium non-magnetic. We find magnetic fields with plasma $\beta \sim 10$ already stabilize and widen the jet head. Furthermore, they are efficiently amplified by a shearing mechanism in the jet head and are strong enough to damp Kelvin–Helmholtz instabilities of the contact discontinuity. The cocoon magnetic fields are found to be stronger than expected from simple flux conservation and capable to produce smoother lobes, as found observationally. The bow shocks and jet lengths evolve self-similarly. The radio cocoon aspect ratios are generally higher for heavier jets and grow only slowly (roughly self-similar) while overpressured, but much faster when they approach pressure balance with the ambient medium. In this regime, self-similar models can no longer be applied. Bow shocks are found to be of low eccentricity for very light jets and have low Mach numbers. Cocoon turbulence and a dissolving bow shock create and excite waves and ripples in the ambient gas. Thermalization is found to be very efficient for low jet densities.

Key words: magnetic fields – MHD – methods: numerical – galaxies: clusters: general – galaxies: jets – radio continuum: galaxies.

1 INTRODUCTION

Extragalactic jets are amongst the most powerful phenomena in the Universe and observable up to high redshift (Miley & De Breuck 2008). Jet activity is generally accompanied by synchrotron emission from relativistic electrons in the magnetized jet plasma, which is most prominently observable at radio frequencies. Thus radio observations provided us with much insight into jet morphology (beams, knots, hotspots, lobes/cocoons), classification into low-power Fanaroff–Riley type I (FR I) and high-power FR II sources (Fanaroff & Riley 1974), magnetic field strengths estimated by minimum energy arguments in the range of a few to several hundreds of microgauss in hotspots (Bridle 1982; Meisenheimer et al. 1989) as well as magnetic field topology from polarization measurements (Bridle & Perley 1984; high-power jets generally show magnetic fields parallel to the jet axis) and age estimates from spectral ageing (Alexander & Leahy 1987; Carilli et al. 1991) of a few $\times 10^7$ years. Extragalactic jets show prominent cocoons, often only partly visible as lobes, with total length to total width aspect ratios mostly between 3 and 10 (Mullin, Riley & Hardcastle 2008). However, it must be cautioned that visible radio emission does not necessarily trace all the bulk plasma, but depends on magnetic field strength and electron acceleration.

The current X-ray observatories *Chandra* and *XMM–Newton* give rise to a complementary view on jets, observing bremsstrahlung radiation from the thermal ambient gas (Smith et al. 2002) and inverse-Compton emission from the jet cocoon (Hardcastle & Croston 2005; Croston et al. 2005), the latter suggesting near-equipartition magnetic fields. These emission processes are less dependent on

⋆E-mail: vgaibler@mpe.mpg.de

microphysics and thus easier to connect with theoretical results and furthermore contain information about the history of these sources.

An extreme example for this is MS0735.6+7421 (McNamara et al. 2005), where radio emission shows a weak source, while the spatially coincident X-ray cavities reveal the true average power of the active galactic nuclei (AGN; $1.7 \times 10^{46}\,\mathrm{erg\,s^{-1}}$), which is a factor of $\sim 10^5$ higher. The jet cocoon displaces the ambient thermal gas and drives a bow shock outwards. Both pV work and the bow shock contain signatures of the jet properties and may be excellent diagnostic tools. Nearly three-dozen clusters were found to have cavities (McNamara & Nulsen 2007) and generally show weak bow shocks (Mach 1–2) with aspect ratios (length/width) not much above unity.

Radio observations of high-power FR II jets show wide cocoons (Mullin et al. 2008), which are partly (and more completely at low frequencies) visible as radio lobes. Both jet head and cocoon–ambient gas interface appear smoother in radio maps (e.g. Cygnus A, Lazio et al. 2006; Pictor A Perley, Röser & Meisenheimer 1997; but also Hercules A, Gizani & Leahy 2003) than they do in hydrodynamic (HD) simulations, and while the emission of synchrotron radiation obviously indicates the presence of magnetic fields their importance for jet dynamics and the contact surface is still unclear.

On the theoretical side, early numerical simulations of supersonic jets (Norman et al. 1982) already exhibited basic structures seen in observations of extragalactic radio sources (working surface, cocoon, bow shock) and showed that pronounced cocoons are properties of jets with much lower density than the ambient medium (light jets), although the slow propagation of the jet makes simulations of these computationally very expensive. With the availability of more computing power and new codes, simulations of the long-term evolution (Reynolds, Heinz & Begelman 2002), in three dimensions (Balsara & Norman 1992; Clarke, Harris & Carilli 1997; Krause 2005; Heinz et al. 2006), of very light (Carvalho & O'Dea 2002a,b; Saxton, Bicknell & Sutherland 2002a; Saxton et al. 2002b; Krause 2003; Zanni et al. 2003; Sutherland & Bicknell 2007) and relativistic jets (Aloy et al. 1999; Komissarov 1999; Rosen et al. 1999; Hardee 2000; Leismann et al. 2005) became possible. Furthermore, effects of magnetic fields were examined (Clarke, Norman & Burns 1986; Lind et al. 1989; Kössl, Müller & Hillebrandt 1990; Hardee & Clarke 1995; Tregillis, Jones & Ryu 2001, 2004; O'Neill et al. 2005; Li et al. 2006; Mizuno, Hardee & Nishikawa 2007; Keppens et al. 2008), although only for relatively dense jets (density contrast $\gtrsim 10^{-2}$). In this paper, we extend the studies of very light jets to include magnetic fields.

To explore the interaction of jets with the ambient intracluster medium and the impact of magnetic fields, we performed a series of magnetohydrodynamic (MHD) simulations of very light jets on the scale of up to 200 kpc (200 jet radii) with a globally consistent magnetic field configuration. A constant ambient density was used to avoid effects of a declining cluster gas density on the structural properties which could contaminate the effect of magnetic fields, while the effects of a density profile previously were described in Krause (2005) for the axisymmetric and three-dimensional case.

After a description of our simulation setup and the numerical method, our results are described: first about the morphology and dynamics, the evolution of the bow shock and the cocoon; then entrainment of ambient gas and the energy budget and finally the magnetic fields and their evolution as well as their impact on morphology and propagation. Results are then discussed and put in context with observational findings.

To compensate for different propagation speeds of jets with differing density contrasts, plots will use the axial bow shock diameter or jet length, where appropriate. 'Full length' refers to the whole simulated length (considering both jets), while 'full width' refers to twice the measured (radial) distance from the axis.

2 SETUP AND NUMERICAL METHOD

2.1 Setup

The idea behind the present study was to explore the behaviour of very light jets with non-dominant magnetic fields in a cluster environment using a plausible global setup for the plasma and the magnetic fields, but still keeping the setup simple enough to see the working physical processes clearly, which is much harder for a complex setup. We performed 2.5D simulations (axisymmetric with 3D vector fields) of both purely HD and MHD jets on the scale of up to 200 kpc with a constant ambient gas density, where density contrasts $\eta = \rho_\mathrm{j}/\rho_\mathrm{a}$ were varied between 10^{-1} and 10^{-4} to see its effects on the simulation. Jet speed, beam radius, sonic Mach number and magnitude of the helical magnetic field (Gabuzda et al. 2008) were kept fixed, thus yielding a kinetic jet power $L_\mathrm{kin} = \pi r_\mathrm{j}^2 \eta \rho_\mathrm{a} v_\mathrm{j}^3$ and plasma $\beta = 8\pi p/B^2$ varying with density contrast. A summary of the parameters is given in Tables 1 and 2. The simulations are labelled by a letter and a numeral, indicating the inclusion of magnetic fields (M) versus pure hydrodynamics (H) as well as their density contrast. Both simplifications – axisymmetry and density distribution – were relaxed in a previous HD study (Krause 2005) and their influence is addressed later in the discussion. The initial gas distribution was randomly perturbed on the resolution scale to break symmetry between both jets.

The bipolar (back-to-back) jets were injected by a cylindrical nozzle (radius r_j, length $2r_\mathrm{j}$) along the Z axis in cylindrical coordinates (Z, R, ϕ), hence allowing for interaction of the backflows in the mid-plane. The jet radius is resolved by 20 cells. Fully ionized hydrogen ($\gamma = 5/3$) was assumed for both the jet and the external medium. A compressible tracer field was advected with the flow, using a value of 1 for the ambient gas, and 0 and -1 for the jets, allowing to trace back the origin of the plasma. Optically thin cooling is included in the code but was switched off, since the cooling

Table 1. Common simulation setup parameters. Nozzle averages are restricted to $R \leq 0.9\,r_\mathrm{j}$ ($\leq 0.8\,r_\mathrm{j}$ for M4 and M4L).

Jet speed	v_j	0.6c
Jet sound speed	c_s	0.1c
Jet radius	r_j	1 kpc
Ambient gas density	ρ_a	$10^{-2}\,m_\mathrm{p}\,\mathrm{cm^{-3}}$
Ambient gas temperature	T_a	5×10^7 K
Jet nozzle magnetic field	$\langle B_\mathrm{p} \rangle$	18.1 μG (M4L: 1.81 μG)
	$\langle B_\phi \rangle$	7.5 μG (M4L: 0.75 μG)

Table 2. Parameters for the different simulation runs. Nozzle averages are restricted to $R \leq 0.9\,r_\mathrm{j}$ ($\leq 0.8\,r_\mathrm{j}$ for M4 and M4L). β values are typical over simulation run.

Run	$\eta = \rho_\mathrm{j}/\rho_\mathrm{a}$	$\langle \beta^{-1} \rangle^{-1}$	t_max (Myr)
M1	10^{-1}	810.	6.7
M2	10^{-2}	81.	10.9
M3	10^{-3}	8.1	16.5
M4	10^{-4}	0.89	47.5
M4L	10^{-4}	36.	50.0

times for our setup ($\gg 10^8$ years) are significantly longer than the simulated time-scale, even for the shocked ambient gas. This choice also makes the simulations scalable, e.g. to other values of the jet radius, which was chosen arbitrarily as $r_j = 1$ kpc.

In the jet nozzle, all HD variables (density, pressure and velocity) are kept constant at all times and a toroidal field $B_\phi \propto \mathrm{sgn}(Z)\sin^4(\pi R/r_j)\,R/r_j$ is prescribed there, being zero outside the nozzle. A dipolar field centred on the origin is used as initial condition for the whole computational domain (magnetic moment aligned with the jet axis) although it is mostly confined to the jet due to the strong decrease in magnitude with distance. For global simulations, the $\nabla \cdot \boldsymbol{B}$ constraint enforces closed field lines, which is satisfied by a dipolar field configuration, but not by the common setup of an infinite axial field, which locally, but not globally, fulfils the constraint. Thus, in our setup, the magnetized jet plasma propagates into the essentially non-magnetic ambient matter. For M3 and especially M4, the magnetic fields become dynamically important and influence the appearance, so another run with lowered magnetic fields was performed in addition (M4L), which is more in line with the other jets. These lightest jets are addressed more specifically in Section 3.7.

The initial magnetic fields in Table 1 are nozzle-averaged initial values. As the poloidal field cannot be kept constant in the nozzle without violating $\nabla \cdot \boldsymbol{B} = 0$, this field can evolve with time due to the interaction with the enclosing cocoon, quickly adjusting to 13 μG (1.5 μG for M4L) but then stays constant. For these nozzle averages, only 90 per cent of the jet radius were considered for M1, M2, M3 and 80 per cent for M4 and M4L to exclude cells at the shearing boundary of the nozzle, where high magnetic fields and opposite field directions can occur, while the core of the jet is unchanged. For plasma β, we use the volume-averaged harmonic mean, as very weakly magnetized regions otherwise would misguidingly dominate the average.

Since the jets are very underdense with respect to the ambient gas and have a high internal sound speed, a reconfinement shock develops already very near the jet nozzle. This shock establishes pressure balance between the jet beam and the cocoon, resulting in a pressure-confined beam. In contrast to freely expanding jets, any imposed opening angle becomes unimportant once the beam is reconfined already near the jet inlet. Hence, in contrast to heavier jets, underdense jets quickly find pressure balance with their environment.

The simulations were run until they reach the boundary of the uniform grid which has 4000×800 or 4000×1600 cells (for M4 and M4L) and the jet radius (r_j) is resolved with 20 cells.

In the following, we will focus only on the MHD jets, as their hydro counterparts are only for comparison (set up exactly as the MHD jets with vanishing magnetic field).

2.2 Method

The simulations were performed using the NIRVANA code (Ziegler & Yorke 1997), which numerically solves the non-relativistic MHD equations in three dimensions in Cartesian, cylindrical or spherical coordinates. It is based on a finite-difference discretization in an explicit formulation using operator splitting and uses van Leer's interpolation scheme, which is second-order accurate. The advection part is solved in a conservative form and the magnetic fields are evolved using the constrained transport method, which conserves $\nabla \cdot \boldsymbol{B}$ up to machine roundoff errors. The code was vectorized and shared memory parallelized (Gaibler et al. 2006) for the NEC SX-6 and SX-8.

3 RESULTS

3.1 Morphology

The density and temperature maps of Fig. 1 show snapshots of all runs at a full jet length of 100 kpc, respectively. In the following, M3 mostly will be used for figures as it has the strongest non-dominant magnetic fields, therefore showing effects of the magnetic fields best and allowing for comparison of features between different figures. The jet backflow blows up a pronounced cocoon, surrounded by a thick shell of shocked ambient matter. Dense ambient gas is mixed into the cocoon in finger-like structures due to Kelvin–Helmholtz (KH) instabilities at the contact surface. Near the jet heads, this instability is suppressed by the magnetic field, which leads to a smoother appearance there. In purely HD simulations, this stabilization is absent.

The cocoon is highly turbulent and vortices hitting the jet beam can easily destabilize, deflect or disrupt it if jet densities are low. The Mach number varies considerably along the beam (Saxton et al. 2002b; Krause 2003) and there is no stable 'Mach disc' as seen for heavier jets – the terminal shock moves back and forth and often is not clearly defined.

Because very light jets only propagate slowly, basically hitting the ambient gas as a 'solid wall', the backflow is strong and the turbulence makes the interaction between both jets in the mid-plane important. Such jets have to be simulated bipolarly to describe the lateral expansion and hence the global appearance correctly. If only one jet were simulated, for very light jets the result would strongly depend on the boundary condition in the equatorial plane (Saxton et al. 2002b).

The surrounding ambient gas is pushed outwards by the cocoon pressure, driving a bow shock outwards. The bow shock for very light jets is different in its shape and strength from that of heavier jets (see Section 3.3). It is additionally changed by a density profile in the external medium (Krause 2005), which increases the aspect ratio with time because η increases at the jet head and thus shows cylindrical cocoons.

3.2 Defining the cocoon

In the following, we not only measure properties of the bow shock, which is easy to pin down, but also of the cocoon. While generally we define the cocoon as the region, which is filled by jet-originated matter (not including the beam itself) this definition has to be made in more detail for the simulation analysis. The strong backflow and the fragile beams of very light jets make the distinction between cocoon and beam difficult, while mixing at the contact discontinuity complicates the assignment of cell to cocoon or ambient matter. While we do not attempt to distinguish between beam and cocoon if not stated explicitly (it only seems necessary for energetic investigations), the distinction between cocoon and ambient matter is necessary especially for the entrainment measurements later and thus is described in more detail in this section, along with the measurement of the cocoon properties.

3.2.1 Cell assignment

Two properties can be used for the distinction between cocoon and ambient matter: the (compressible) tracer field and the toroidal magnetic field. Tracer field values of 1 and above indicate undisturbed and shocked ambient matter. This is available in all simulations, but mixing with jet matter at the contact discontinuity (due to finite

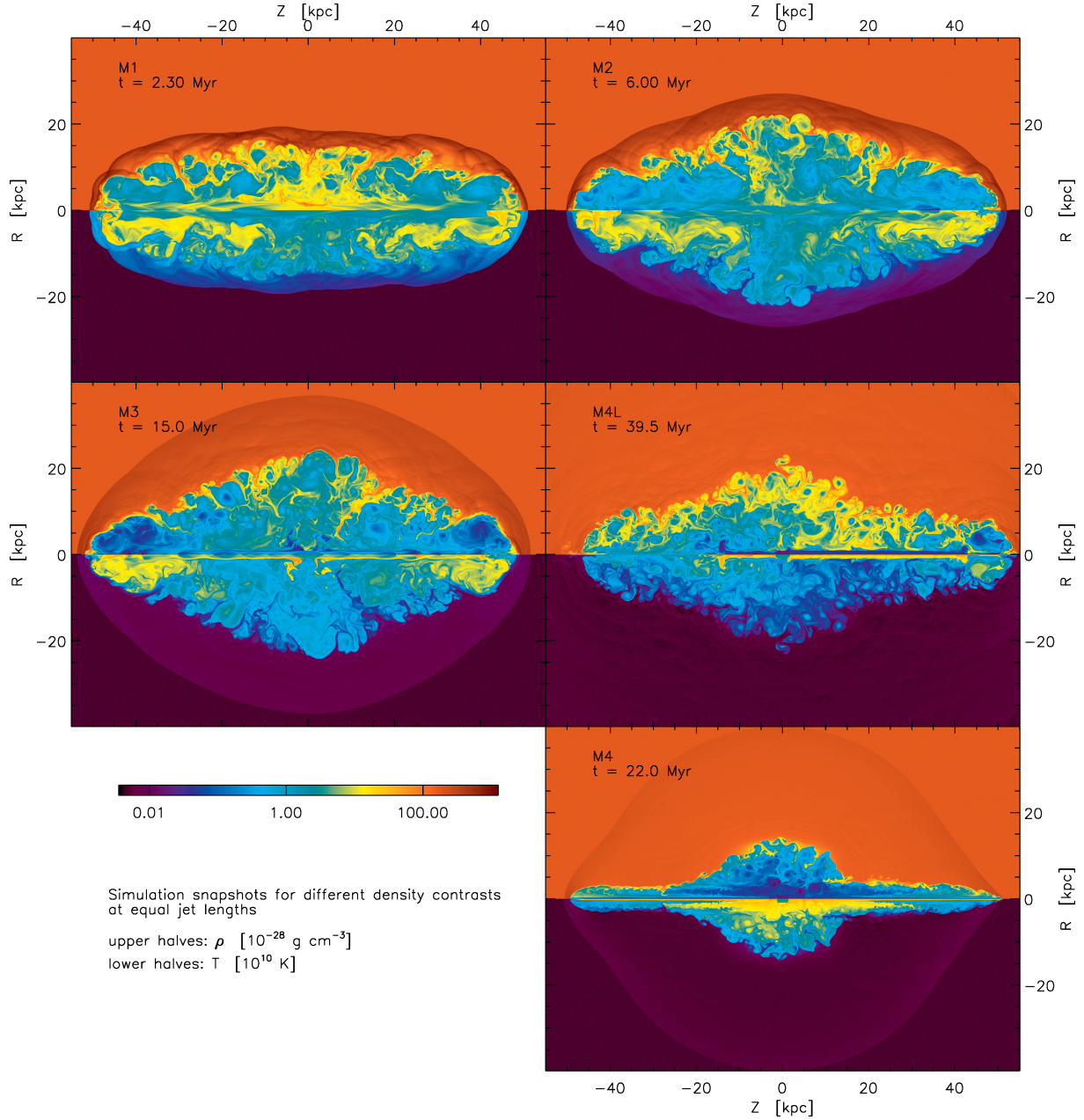

Figure 1. Density and temperature for all runs, each at a jet length of ≈100 kpc. The upper halves of each panel show the logarithmic density in units of 10^{-28} g cm^{-3}, the lower halves show the logarithm of temperature in units of 10^{10} K. Panels additionally are labelled by their respective time.

resolution) lowers the tracer and thus requires a threshold value. The cocoon mass is especially sensitive to this threshold value, as the density of the ambient gas is much higher and thus causes large changes of the cocoon mass if the border is shifted. Fig. 2 shows the cocoon mass for a range of tracer thresholds. The injected mass at this time is only 4×10^6 M$_\odot$; measured mass above this value is the entrained ambient gas mass.

In contrast, the toroidal field strength can be used for separation, as the toroidal field is zero initially in the ambient medium and is conserved independent from the other field components. Fig. 3 shows the cocoon mass depending on the toroidal magnetic field threshold. Using this method, even cells with only a small mass fraction of jet matter can be assigned to the cocoon. There is a clear break visible, but the cocoon mass continuously increases for lower threshold values until machine accuracy is reached.

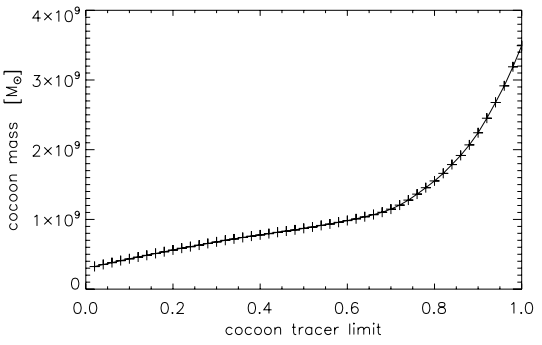

Figure 2. Cocoon mass depending on tracer field threshold (mass of all cells with tracer below the threshold), for simulation M3 at $t = 15$ Myr.

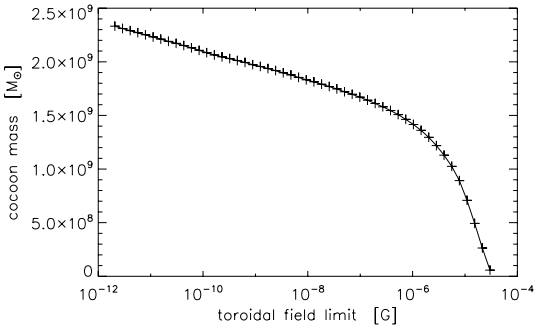

Figure 3. Cocoon mass depending on toroidal field threshold (mass of all cells with toroidal field magnitude above the threshold). Simulation M3 at $t = 15$ Myr.

This has two major problems. First, it naturally is not available for the pure hydro simulations and thus cannot be used to compare HD with MHD simulations. Secondly, the high sensitivity to jet matter is not a real advantage, as the mass values do not nicely converge and we have to choose a threshold. In the following, we will use a tracer threshold of 0.5 which is available for HD and MHD models and gives cocoon masses that do not strongly depend on the tracer threshold. Furthermore, it selects the regions one would consider cocoon also by looking at the other physical variables.

3.2.2 Shape measurement

To characterize the width of the cocoon, we checked four different measures, which will generally give different results due to the ragged shape of the contact surface. Widths are measured from the symmetry axis ($R = 0$, jet channel) and thus are only 'half widths'. Fig. 4 shows the temporal evolution of the cocoon width definitions:

(i) maximum width – measured at the maximum R position of a cocoon cell;
(ii) average width – Z-averaged over the full jet length;
(iii) QB width: measured at one quarter the full jet length backwards of the jet heads;
(iv) spheroid width – semiminor axis of a spheroid with a volume equal to the cocoon volume and the semimajor axis equal to half the full jet length.

The QB width is clearly much dependent on vortices near the contact surface and not very straight. Despite that, it grows similar to the Z-averaged width, which mostly has the lowest width value of all four definitions. The spheroid width lies between the maximum

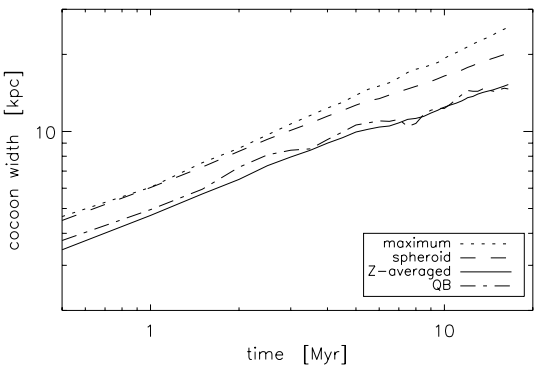

Figure 4. Evolution of the cocoon width for different width definitions for simulation M3. A tracer limit of 0.5 was used for cell assignment.

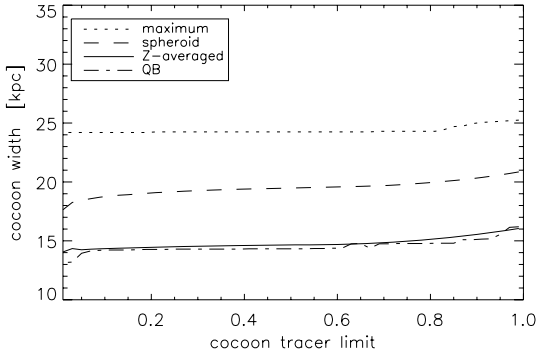

Figure 5. Cocoon width for different width definitions as function of the used tracer limit. For simulation M3 at 15 Myr.

width and the Z-averaged width. All of theses measures can be approximated by power laws, although with somewhat different parameters.

In contrast to the cocoon mass, the cocoon shape does not depend strongly on the tracer limit that is used for its determination (Fig. 5). For limits around 0.5, the difference between width definitions is larger than the dependence on the tracer limit.

3.3 Evolution of bow shock and cocoon

3.3.1 Cocoon pressure evolution

The low jet density has two main consequences for the evolution of the cocoon pressure: one is the lower jet power (for a fixed jet bulk velocity), which results in a lower cocoon pressure and a generally weaker bow shock. The other is the slow jet head propagation, which lowers the propagation time-scale compared to the dynamical time-scale of travelling pressure waves within the cocoon. Pressure waves from the jet head together with waves induced by turbulent motion and mixing in the cocoon, try to establish pressure balance within the cocoon and between cocoon and ambient gas, driving the lateral expansion of the cocoon.

Fig. 6 shows pressure maps of jets with $\eta = 10^{-1}$ and 10^{-3} at the same lengths. The cocoon of the heavier jet is overpressured by a factor of 20 with respect to the ambient gas, while being a factor of only 1.5 for the lighter jet (and 4.9 for this jet at the time of the M1 image).

The strong evolution towards pressure balance is responsible for the much less pronounced high-pressure regions between Mach disc

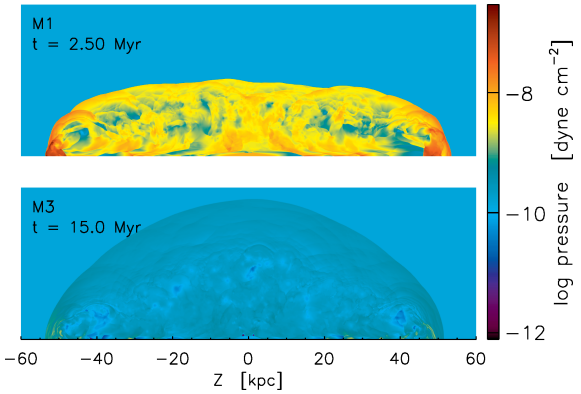

Figure 6. Pressure maps in logarithmic scaling for simulation M1 and M3 at equal lengths.

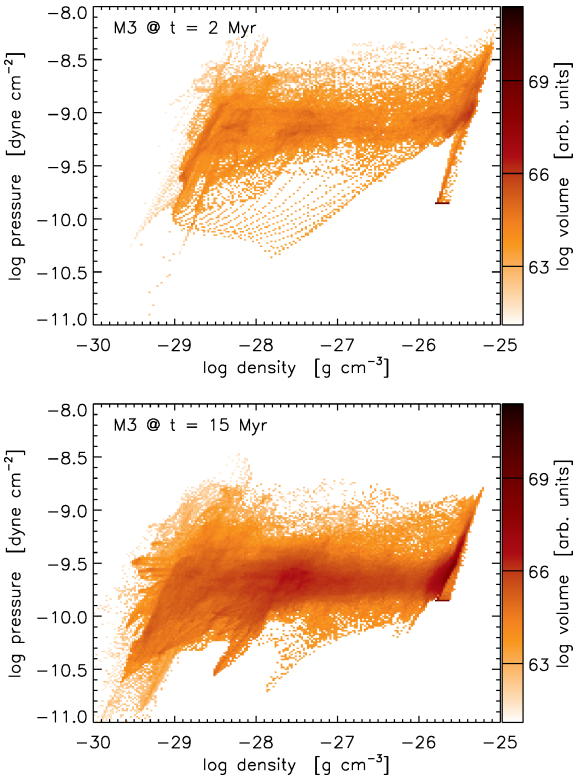

Figure 7. Pressure versus density histogram for the M3 jet after 2 and 15 Myr. Volume-weighted counts, pressure and density are shown logarithmically.

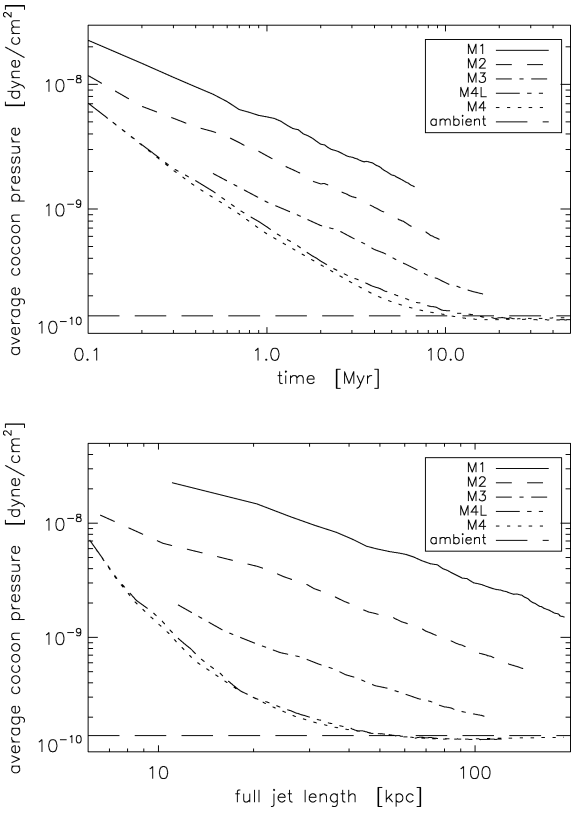

Figure 8. Evolution of the volume-averaged cocoon pressure as function of time or the jet length for the different models. The cocoon is defined by a tracer limit of 0.5. MHD models are shown in thick lines, corresponding hydro models in thin lines, the ambient pressure is indicated by the long-dashed line for comparison.

and the advancing bow shock. The bow shock has an elliptical shape with less directional dependence of its strength, more similar to an overpressured bubble, although it is still stronger in axial direction (see Section 3.3.2).

The quick pressure adjustment can also be seen in the pressure–density diagrams of Fig. 7. The ambient gas is described by the patch near (−26, −10), the jet nozzle by the cells around (−29, −10). Adiabatic compression and expansion leads to the oblique and longish features present at different positions. Top right of the jet nozzle position are the cocoon grid points, which spread over a large range of density to the right because of mixing with shocked ambient gas, which is the elongated feature top right of the ambient gas position. Comparing the two different simulation snapshots, we find that the pressure distribution is quickly adjusting towards the external pressure, in agreement to the findings in Krause (2003), and the cocoon is not strongly overpressured anymore.

Another view on this is the average cocoon pressure, shown in Fig. 8, which has a power-law-like behaviour. For the three models M1, M2 and M3, it strikingly decreases with the reciprocal jet length (Table 3). While M1 at the end of the simulation is still very overpressured, the cocoon pressure of M3 is already near the ambient gas pressure.

M4 and M4L seem to deviate from this behaviour. At the beginning, this is mainly a consequence of the longer lasting relaxation from initial conditions, where strong shocks are thermalized efficiently, increasing the pressure in the early 'cocoon bubble' and because the early phase is shown with higher time resolution. After a jet length of 20 kpc has been reached, they fit into the behaviour of the other simulations, but, as they soon reach the ambient pressure, settle to its value.

It is clear that the cocoon pressure cannot drop much below the ambient pressure and thus approaches its value. At this point, we expect the bow shock to softly turn into an ordinary sound wave. This is just about to happen in the last snapshots of M4 and M4L, where there is only a very weak density jump, corresponding to Mach 1.05. The exact value of the average cocoon pressure is insensitive to the exact definition of the cocoon (see Section 3.2), but can drop slightly below the ambient pressure due to pressure variation within the cocoon (which can still be as strong as a factor of 2).

The past bow shock is not the only sound wave testifying to the expanding cocoon. Already much before the shock decays, waves and ripples can be seen in the shocked ambient gas (Fig. 9).

3.3.2 Bow shock

The quick decrease in cocoon pressure naturally affects the strength of the bow shock as it is this pressure that drives the shock laterally. Fig. 10 shows the temporal evolution of the bow shock strength, in terms of external Mach numbers, for the forward direction (at $R = 0$) as well as the lateral direction (at $Z = 0$) for jets with different density contrasts.

The bow shocks in forward direction are always stronger than the sideways shocks due to the direct impact of the jet on to the ambient gas. The lighter jets have a much weaker bow shock in all directions and the differences between the axial and lateral direction are much less pronounced. The axial diameter of the bow shock grows as a power law with exponents ≈0.65 (Fig. 11 and Table 3). For the

Table 3. Power-law exponents for the bow shock and cocoon evolution.

Model	Bow shock full length $\propto t^p$ ≥30 kpc	Bow shock width $\propto t^p$ ≥15 kpc	Cocoon full length $\propto t^p$ ≥30 kpc	Cocoon average width $\propto t^p$ ≥5 kpc	Average cocoon pressure $\propto l^p$
M1	0.63	0.64	0.64	0.59	−0.99
M2	0.63	0.61	0.64	0.52	−1.04
M3	0.68	0.65	0.71	0.39	−0.95
M4L	0.69	0.71	0.64	0.24	–
M4	0.80	0.71	0.82	–	–

Note. The exponents p in the table are fits to power laws as function of time (for the lengths and widths) or as function of full jet length (for the average cocoon pressure), considering only the data points which match the criterion in the third line. A minus (−) denotes that no reasonable power-law fit could be done.

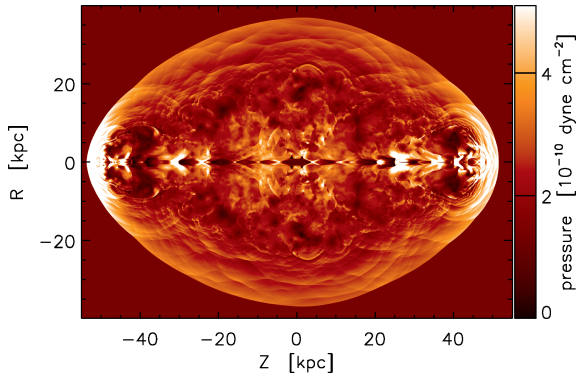

Figure 9. Linearly scaled pressure map of M3 at 15 Myr. Values above 5×10^{-10} dyne cm^{-2} are clipped.

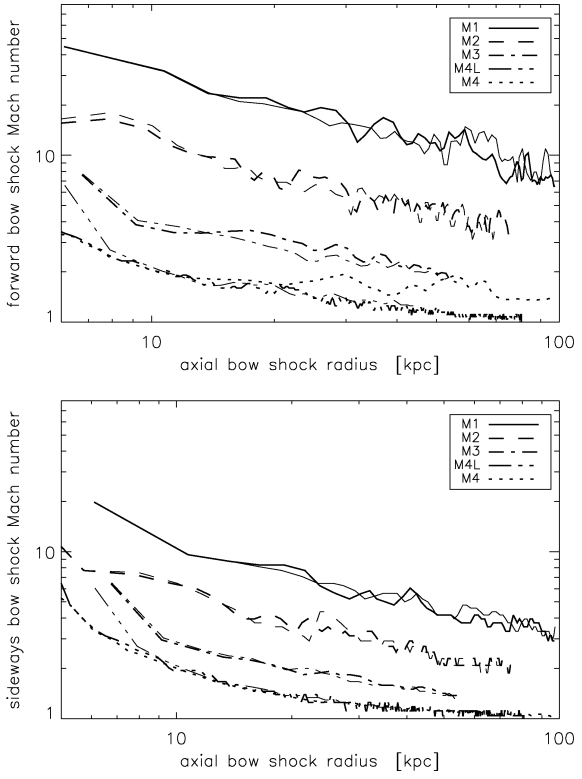

Figure 10. Evolution of the forward (top panel) and sideways (bottom panel) bow shock strength as a function of the monotonically increasing axial bow shock radius. Thick lines are MHD models, thin lines the corresponding hydro models for comparison.

lateral propagation, we find similar exponents. This behaviour agrees with self-similar jet models (Falle 1991; Begelman 1996; Kaiser & Alexander 1997; Komissarov & Falle 1998) and the spherical blast-wave approximation (Krause 2003), which predict an exponent of 0.6. At very early times and lasting longer for the lighter jets, we find lower exponents, as for a Sedov blast wave ($l \propto t^{0.4}$) from the initial conditions.

The lighter jets have generally lower Mach numbers, as their kinetic power is lower, thus showing smaller bow shock velocities. The aforementioned analytical models yield an expansion speed

$$v(r) = k \left(\frac{L_\mathrm{j}}{\pi \rho_\mathrm{a}}\right)^{1/3} r^{-2/3} = k\, v_\mathrm{j}\, \eta^{1/3} \left(\frac{r}{r_\mathrm{j}}\right)^{-2/3}, \qquad (1)$$

that directly translates into the bow shock Mach number and describes the scaling behaviour of the simulations reasonably well (L_j: jet power). We find values for k between 1.5 and 2 in axial direction and between 0.5 and 2 (M4L) in lateral direction, the latter being increasingly higher for lighter jets.

A clear deviation from this behaviour is M4 at $t > 10$ Myr in axial direction. The bow shock propagates much faster due to the formation of a nose cone. The strong toroidal magnetic field collimates the jet, suppresses the pronounced backflow of M4L, and the Lorentz force of the radial current gives the jet additional thrust for the propagation (see 3.7). The other light jets (M3 and M4L) may also propagate somewhat faster due to their appreciable magnetic fields.

3.3.3 Cocoon

As the jet pushes the bow shock forward in axial direction, the cocoon length grows similar to the bow shock length (Fig. 12), showing a power-law behaviour with similar exponents. Again, M4 shows a higher exponent (0.82) due to its additional thrust support in the nose cone. There might also be a slightly faster propagation for the M3 jet, where the magnetic field is not too much below equipartition at the jet inlet (see Fig. 2), although this might also be just a temporal effect due to the jet–cocoon vortex interaction.

The cocoon width, in contrast, shows different power-law exponents depending on the density contrast, after the start-up phase is over. We find exponents of 0.59 (M1), 0.52 (M2), 0.39 (M3) and 0.24 (M4L) for the different models (Table 3). Thus, there seems to be a clear trend of decreasing exponents for lower jet densities, which holds true for all our cocoon width measures (Fig. 13). Widths approaching an asymptotic value might mimic a similar behaviour, but so far this is beyond our simulation data (except for M4). It seems reasonable that this is due to less overpressured cocoons for lighter jets, as it is the cocoon pressure that drives the lateral cocoon

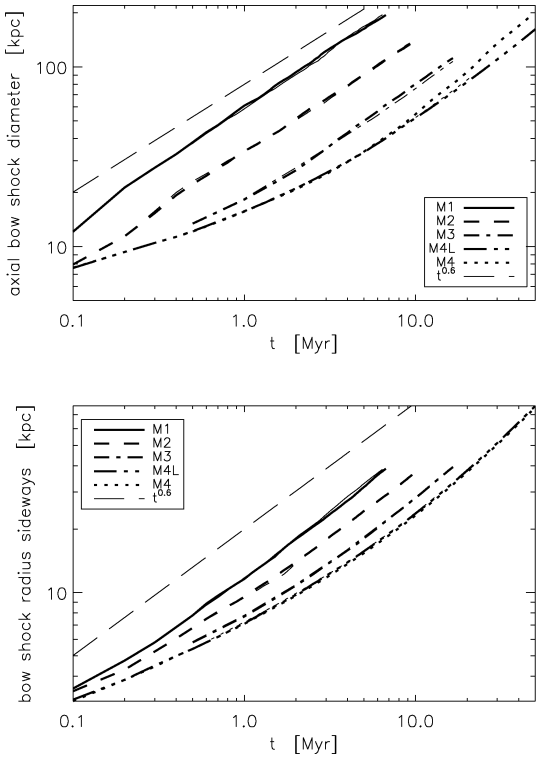

Figure 11. Propagation of the bow shock in axial (top panel) and lateral direction (bottom panel) for the simulated models as function of time. Thick lines are MHD models, thin lines the corresponding HD models. A power law $\propto t^{0.6}$ is shown for comparison as long-dashed line.

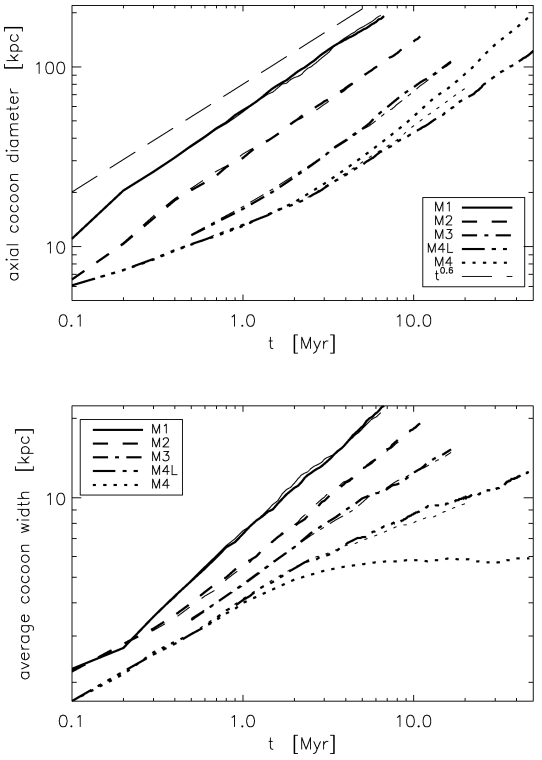

Figure 12. Time evolution of the cocoon: full length and average width as function of time. MHD models in thick lines, corresponding hydro models in thin lines.

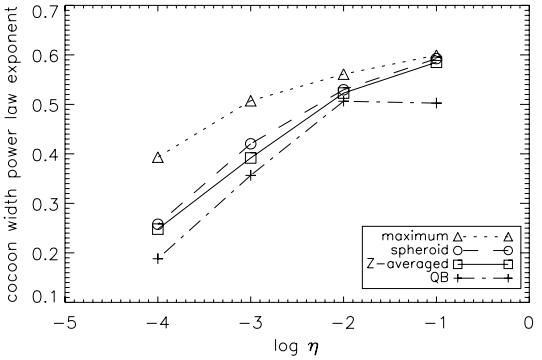

Figure 13. Power-law exponents for cocoon widths as function of density contrast. Fits considered only data points where width $\gtrsim$5 kpc.

expansion (Kaiser & Alexander 1997; Carvalho & O'Dea 2002b). If the cocoon pressure equals the ambient pressure, the sideways expansion of the cocoon would come to an end.

Another consequence of this is the lateral bow shocks, compared to the corresponding cocoon width, being much further away for light jets (Fig. 14), as found by Zanni et al. (2003) too. Hence, except for the H1/M1 models, the thick layer of shocked ambient gas grows continuously.

The expansion of the cocoon for M4 is much different. After the initial phase, the cocoon width settles down to a constant value and does not grow anymore. This is a consequence of the suppressed backflow in the nose cone, which then cannot inflate the cocoon anymore.

All simulations with non-dominant magnetic fields show pronounced turbulence in their cocoons. This is evident from Fig. 15, which shows the vector fields of velocity and poloidal magnetic fields in line integral convolution (LIC) representation. The LIC technique (Cabral & Leedom 1993) allows the fine-grained depiction of vector fields, especially suitable for turbulence, where structures even on smallest scales are present due to the turbulent cascade. We extended this to show the field magnitude, additionally, decomposing the information into brightness (showing the field direction as stream lines) and colour (field magnitude) in HLS colour space (hue, lightness, saturation).

Cocoon turbulence is driven by quasi-periodic 'vortex shedding' (Norman et al. 1982) in the jet head, which injects vortices into the cocoon. As these vortices move around and interact, vortex shedding affects the whole cocoon and drives its turbulence. While it occurs in our heavier jets too, narrow cocoons suppress vortex interaction and the establishment of turbulence. We note that there may be feedback on the driving mechanism, as cocoon vortices perturb the jet beam and thus influence the vortex-shedding process itself.

3.3.4 Aspect ratio

A characteristic property of the bow shock or cocoon is their aspect ratio $\mathcal{R}$ = length/width (Fig. 16). Dependent on the density contrast, after a short initial phase of spherical expansion ($\mathcal{R} \approx 1$), the bow shock aspect ratios grow but converge for large bow shock diameters, approaching 1 for lighter jets ($\mathcal{R} = 1.4$ for M3 and 1.1 for M4L). This means, the bow shock approaches a spherical shape for very light jets. Once again, M4 is different, as the propagation in axial direction is faster, yielding significantly higher aspect ratios than M4L.

The aspect ratios for the cocoons generally increase with jet length and are at early times systematically lower for the lighter

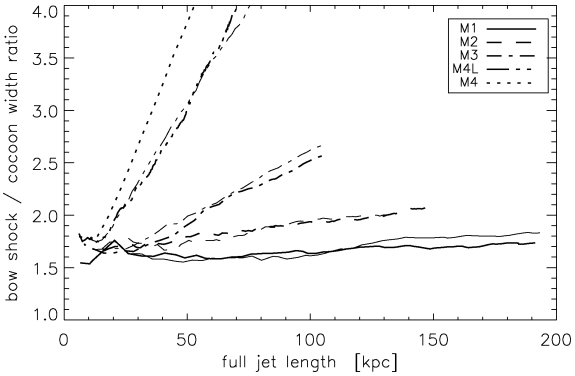

Figure 14. Bow shock/cocoon width ratio over time for the different simulations as function of the full jet length. MHD models in thick lines, corresponding hydro models in thin lines.

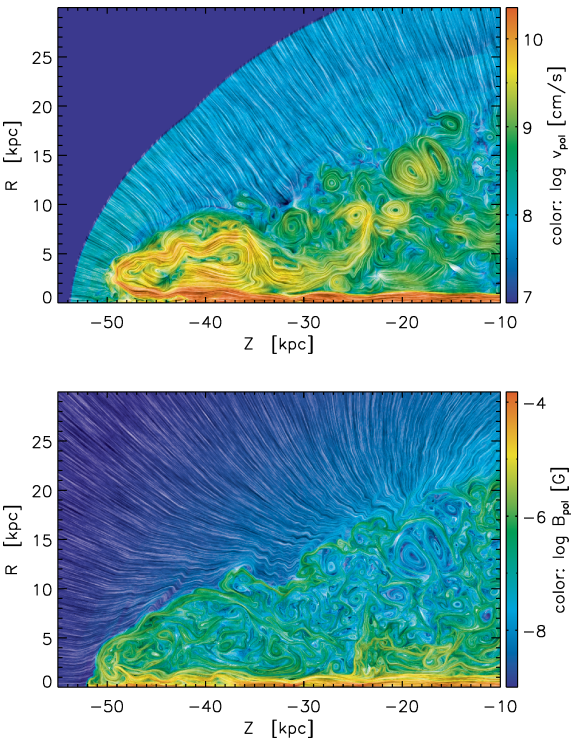

Figure 15. Velocity field (upper panel) and poloidal magnetic field (lower panel) around the jet head, displayed in LIC representation to show the small-scale vector field structure. The colours show the vector field magnitude, while the brightness modulation shows the field lines.

jets. However, the light jets soon increase their aspect ratio (earlier for lighter jets) and then at later times show aspect ratios even higher than their heavy counterparts. As for the cocoon width evolution, we argue that this is due to cocoons, which come to pressure balance with the ambient gas earlier, so that lateral cocoon expansion stalls, but the axial propagation is still growing self-similarly. By comparing Fig. 8 and Fig. 16, one sees that once a source approaches pressure balance with its environment, it drops out of self-similarity and increases its cocoon aspect ratio. For M3, this happens already early, while it does not happen for M1 until the end of the simulation.

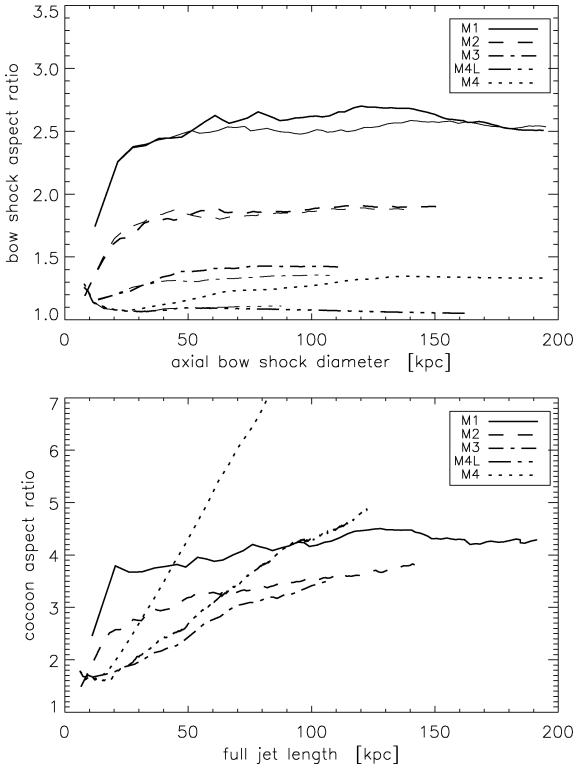

Figure 16. Aspect ratios $\mathcal{R}$ of bow shock (upper panel) and cocoon (lower panel) over full length. For the cocoon aspect ratios, the hydro models are omitted for clarity.

3.4 Entrainment

The jet backflow at the contact surface between the cocoon and the ambient gas makes it KH unstable, and thus creates fingers of dense ambient matter that reach into the cocoon and are entrained. In numerical simulations, this entrained gas is additionally mixed with the jet plasma due to finite numerical resolution. The amount of entrainment can be measured in terms of the cocoon mass since the mass of jet plasma usually is small compared to the measured cocoon mass. Although the exact numbers depend on the exact cocoon measurement definition (Section 3.2), this seems to be a reasonably robust method.

Fig. 17 shows the time evolution of the cocoon mass. The entrained mass grows with a power law exponent only slightly below

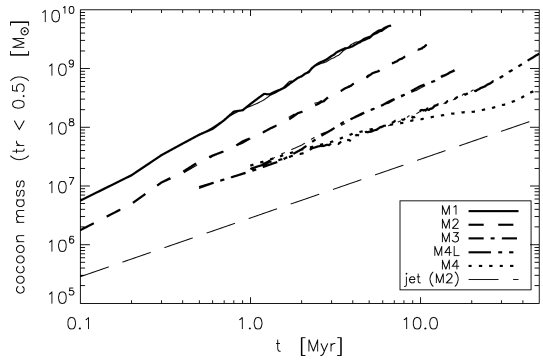

Figure 17. Evolution of the cocoon mass as measure for the entrainment of dense ambient gas. The long-dashed line gives the injected jet mass M_j for the M2 run for comparison ($M_j \propto \eta t$). MHD models as thick lines, corresponding hydro models as thin lines.

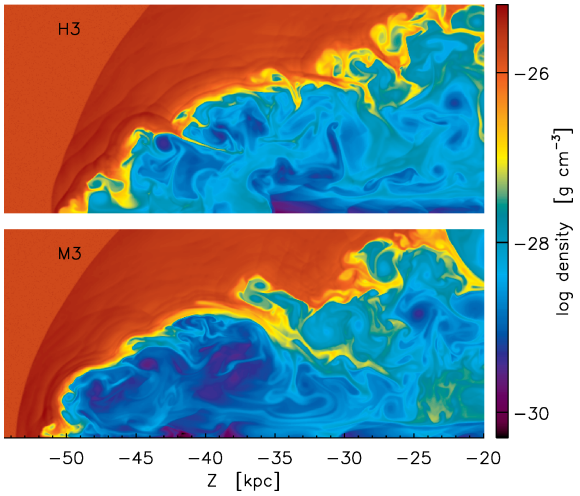

Figure 18. Comparison of hydro (H3) and MHD (M3) simulations at 15 Myr. The jet head region is much more pronounced, KH instabilities are damped, and the jet has propagated a bit further.

the exponent of the cocoon volume, showing a slowly decreasing but roughly constant fraction (5–10 per cent) of the initial mass in the occupied volume. However, there is no difference visible between purely HD and MHD simulations in the entrained mass, as would have been expected. The reason for this is the missing stabilization of the contact surface, which is discussed later. However, it is evident from M3 in Fig. 18 that the entrainment in the jet head is significantly smaller: the mass in a cylindrical volume ($Z \in [-45, -35]$ kpc, radius 4 kpc) in the head region of M3 is $3 \times 10^5\,\mathrm{M}_\odot$ without magnetic fields (H3), compared to $9 \times 10^4\,\mathrm{M}_\odot$ in the magnetized case, which is more than a factor of 3 lower. Hence, entrainment is significantly suppressed in the jet head, but no change could be measured regarding the whole cocoon volume.

3.5 Energy budget

From the quick balancing of pressure within the cocoon, one might expect a strong conversion of (kinetic) jet power to thermal energy. This, in fact, is measured for our simulations.

Fig. 19 shows the increase in thermal energy as fraction of the total injected power. Already for the heaviest jet (M1), most of the injected (kinetic) power appears as thermal energy due to compression and irreversible entropy generation at shocks. The thermal fraction increases not only with time, but is also much stronger for the lighter jets, where a thermalization of $\gtrsim$80 per cent is reached.

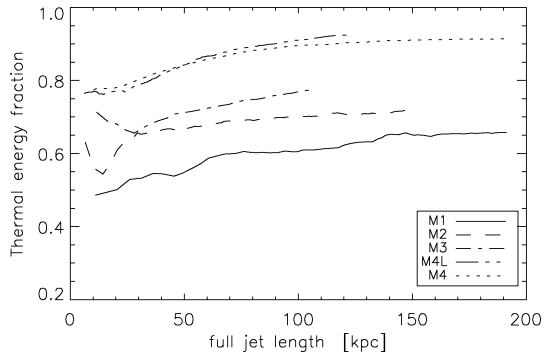

Figure 19. Gains in thermal energy as fraction of the measured total injected energy, as function of the full jet length.

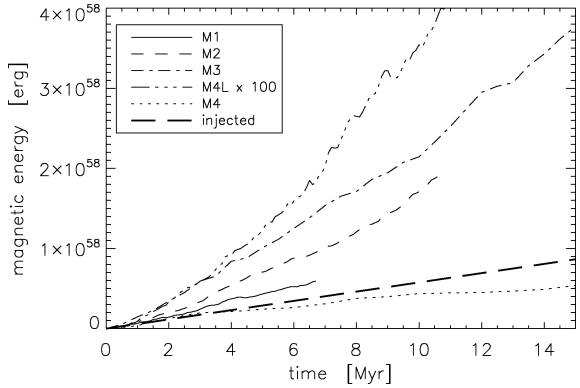

Figure 20. Evolution of the magnetic energy with time. The long-dashed line shows the injected amount of magnetic energy. For the case of M4L, magnetic energy was multiplied by 100 to account for the 10 times smaller field strengths.

Half of the thermal energy gain is found in the cocoon and half in the (shocked) ambient gas. O'Neill et al. (2005) find ≈40 per cent of the jet power in the thermal ambient gas for their 3D jets with density contrast 0.01 in a uniform atmosphere, while in our simulations we find ≈35 per cent, which is quite good agreement.

Magnetic energy only has a very small contribution (below 1 per cent), except for M4, which is magnetically dominated and which has a magnetic energy contribution rising up to 5 per cent. More than 90 per cent of the magnetic energy is located in the cocoon. For all runs except M4, the magnetic energy that is actually measured is significantly larger than the injected magnetic energy (this effect is stronger for the lighter jets) and it grows faster than just linearly in time – approximately with a power-law exponent of 1.2 (Fig. 20). Hence, other forms of energy seem to be converted into magnetic energy. For M4, the measured magnetic energy is lower than expected from the nozzle values, which may indicate that the additional thrust in the nose cone actually consumes magnetic energy.

The remaining fraction is kinetic energy, which is decreasing more and more with lower jet density. Although the jet beam is the only energy input to the system (at the nozzle), its contribution to the total kinetic energy is 10 per cent or less, and 50 to 30 per cent is in the cocoon. The remainder, 50 to 70 per cent, comes from the outward moving shocked ambient gas.

3.6 Magnetic fields

Magnetic fields are not only passive properties of the jet plasma, but an active ingredient for the dynamics. One parameter describing this is the ratio between thermal and magnetic pressure of the plasma ($\beta = 8\pi p/B^2$). For the simulations described here, we used a fixed value for jet speed, Mach number and magnetic field. Thus, the plasma β cannot be constant throughout the different runs (see Table 2). While M1 and M2 have passive magnetic fields, M3 and M4L have fields with significant impact, and for M4 they are even dominant.

The helical field configuration in the jet initiates an intriguing interplay between kinetic and magnetic energy. Although the jet matter is injected without any rotation, the Lorentz force from the helical field generates a toroidal velocity component, as also found by Kössl et al. (1990). This effect is stronger for the runs with stronger magnetic fields (lower plasma β). The rotation does not originate from persisting angular momentum from the jet formation,

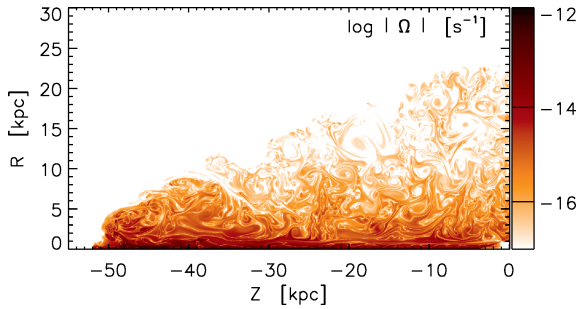

Figure 21. Angular velocity $|\Omega| = |v_\phi|/R$ in units of s^{-1}, scaled logarithmically. Note that there is a strong decline from the beam to the backflow.

which should be very small due to the expansion of the jet. Also, it is not continuous throughout the beam and even changing sign at some internal shocks and interaction with cocoon vortices.

When the plasma reaches the terminal shock, it flows away from the axis radially and turns back, forming the backflow that inflates the cocoon. Rough conservation of angular momentum l then produces a radially declining angular velocity $\Omega = l/R^2$ (differential rotation; Fig. 21). Writing the induction equation in cylindrical coordinates,

$$\frac{\partial B_\phi}{\partial t} = -R\,\left(\boldsymbol{u}_\mathrm{p}\cdot\nabla\right)\frac{B_\phi}{R} - B_\phi\nabla\cdot\boldsymbol{u}_\mathrm{p} + R\,\left(\boldsymbol{B}_\mathrm{p}\cdot\nabla\right)\Omega, \qquad (2)$$

it becomes evident that this shearing transforms poloidal field B_p into toroidal field B_ϕ, also transferring kinetic energy into magnetic energy, which explains why the contribution of magnetic fields to the total energy is higher than its injected contribution.

We note that this creation of toroidal field in the jet head is not an artefact of axisymmetry, but merely a consequence of allowing 3D vectors in the simulation ($\boldsymbol{u}$ and $\boldsymbol{B}$). We do not expect this to be much different in full 3D, apart from a naturally more complex structure in the details. What, in contrast, most probably is an artefact of axisymmetry is the persistence of the toroidal field component in the cocoon. The cocoon plasma is highly turbulent (Section 3.3.3) with relatively little systematic motion, which is an intrinsically 3D phenomenon. This can easily convert toroidal and poloidal field into one another, establishing some dynamical equilibrium between those components, but maintaining the overall field strength.

Comparing purely hydrodynamical models with the MHD models (Fig. 18), we find that the global properties, such as bow shock and cocoon sizes, are generally robust if the magnetic fields are not dominant (as with M4). The details, though, are different. While the hydro models show a ragged contact surface between jet plasma and ambient gas due to Kelvin–Helmholtz (KH) instabilities excited by the backflow, the MHD runs show a pronounced jet head, which is clearly more stable, since the KH instability is damped by the magnetic fields (e.g. Miura & Pritchett 1982). Magnetic tension acts as a restoring force on the growing instabilities, suppressing entrainment of ambient matter and 'fingers' of dense gas reaching into the backflow, which is evident from the clearly lower average density in the jet head region. The stabilizing effect appears at $\beta \sim 10$ in the jet head. For the simulations with weaker fields, there is no notable difference between the magnetized and the pure HD case.

Damping of the KH instability by magnetic fields, however, only works with the field component parallel to the instability wave vector, which in turn means that in axisymmetry only the poloidal magnetic field can damp the instabilities at the contact surface.

Although the earlier mentioned shearing mechanism amplifies magnetic fields and should therefore provide even more damping of KH instabilities, we cannot see this effect further away from the jet head, because in axisymmetry the backward reaction (toroidal to poloidal) cannot work and thus the poloidal component becomes too weak (Figs 15 and 22). As the magnitude of the magnetic field in the cocoon is as strong as in the jet head, it seems reasonable that with balanced magnetic field components in reality, the contact surface could be stabilized.

The toroidal field B_ϕ is directly related to the generating current $\boldsymbol{j}_\mathrm{p}$, which is shown in Fig. 23 as field lines. Our toroidal field setup describes a situation where the poloidal currents leave the nozzle axially in the jet core, turning back in the sheath. As the backflow develops, the poloidal current flows along the contact surface with typical integrated currents of several 10^{18} A (Camenzind 1990; Blandford 2008). The toroidal field in the cocoon, built up by the shearing in the jet head, seems to form its own current circuits. The gross radial behaviour $B_\phi \propto R$ (Figs 24 and 25) can be attributed to the relatively uniform distribution of the axial current through the planes perpendicular to the jet beam.

If the toroidal field is strong in the jet head region, the Lorentz force $f_\mathrm{L} = \boldsymbol{j} \times \boldsymbol{B}/c$ produces additional thrust for the jet propagation due to the strong radial current component, which is evident for M4, showing a pronounced nose cone, and may also explain the slightly faster propagation of M3 with respect to H3 (Fig. 12).

Inside the beam, the magnetic field stays mostly poloidal, as injected, but near the terminal shock it is compressed axially, directed off the axis and sheared, producing strong toroidal field loops (Fig. 26).

Finally, we turn to volume-weighted 2D histograms of magnetic pressure $p_\mathrm{m} = B^2/8\pi$ and thermal gas pressure p in Fig. 27, where the contributions from only the jet beam and all the jet plasma are shown separately.

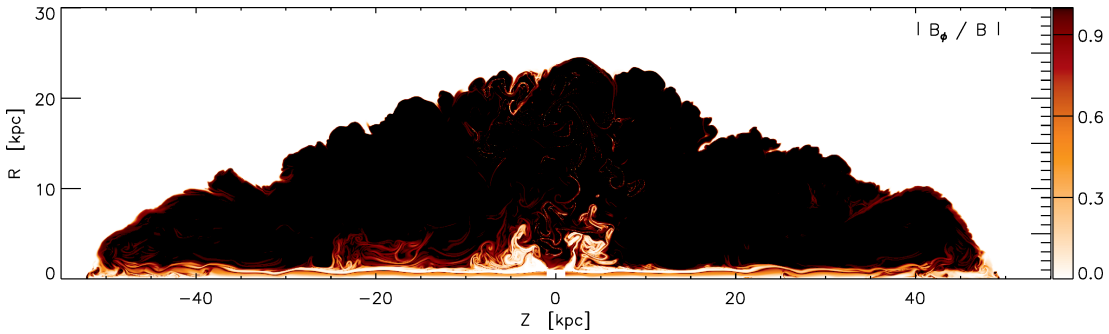

Figure 22. Fractional contribution of toroidal field to the total magnetic field. Simulation M3 at 15 Myr.

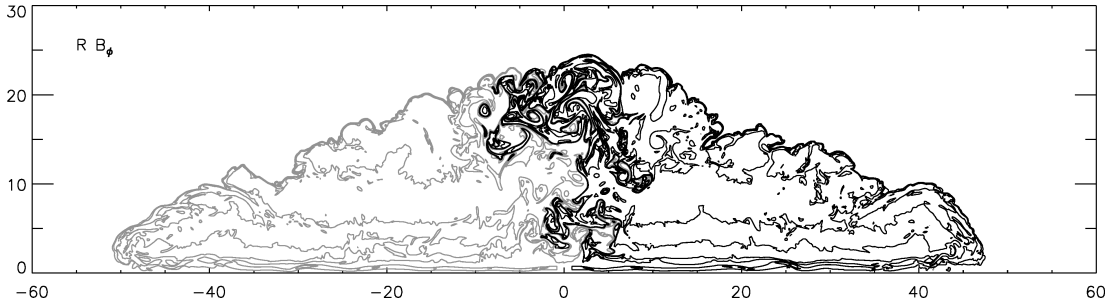

Figure 23. Poloidal current field lines (contours of RB_ϕ). Grey: negative values, black: positive values. Model M3 at $t = 15$ Myr.

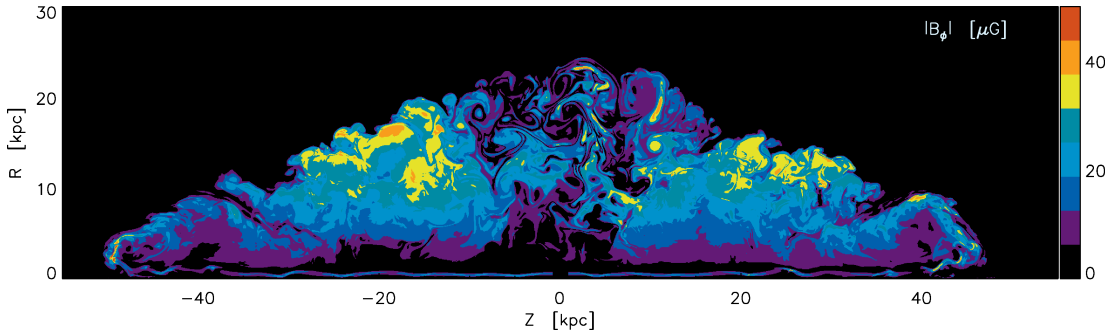

Figure 24. Toroidal magnetic field magnitude for M3 at 15 Myr. The right jet has positive toroidal field, the left jet has negative sign.

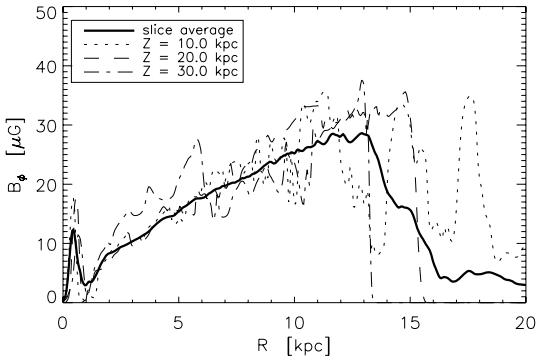

Figure 25. Toroidal field B_ϕ in three slices parallel to the mid-plane, and the average of the whole region $Z = 10 - 30$ kpc. Outside the jet radius $r_j = 1$ kpc, the toroidal field shows a roughly linear increase with R. Although in every slice B_ϕ drops to 0 at $R \approx 1$ kpc, the average does not drop to 0 (and thus is a bit misleading), as the positions are slightly offset for different slices.

The jet nozzle is located at ($\log p$, $\log p_m$) $\approx (-10, -10.5)$ as a vertical line (constant pressure, but radially varying magnetic field). As the matter flows through the beam, internal shocks (cf. Figs 6 and 18) cause strong changes in pressure whereas the plasma β remains unchanged (magnetic field is compressed with the plasma), leading to lines originating from the nozzle location parallel to the overplotted β = constant lines. The plasma β somewhat increases along the beam when it interacts with the cocoon vortices, and thus creates some down-shifted parallels. There is no clear separation between the beam and the enclosing cocoon in the beam-only diagram, hence both shear layers of the beam and cocoon gas are contained in the wide area below $\beta = 10$. Still, there are strong pressure changes indicated by the wide horizontal distribution.

The distribution of cocoon cells widely spreads both to higher and lower magnetic fields from this area. The pronounced trail downwards is the transition to the ambient gas through entrainment; since the ambient gas is essentially unmagnetized, it is located even below the lower border of the figure (Fig. 27). The radial increase of magnetic field in the cocoon yields the extension towards lower plasma β (see also Fig. 28). The spiky features around $\beta \sim 2$ are single vortices in the outer parts of the cocoon, where the pressure drops towards the centre due to centrifugal forces together with a slight increase of toroidal field. Altogether, the spread of the cocoon cells is considerably larger in magnetic pressure than in thermal pressure.

The situation shown in Figs 27 and 29 is typical for the time evolution of these diagrams. Clearly, some features are appearing, changing and disappearing continuously, such as individual internal shock lines or the cocoon vortex spikes. The general structures in the diagrams persist at all times. There are, however, two systematic changes with time. First, the 'cocoon bump' in Fig. 29 ($\log \beta \sim 1$) grows due to cocoon expansion, eroding the 'ambient bump' ($\log \beta \sim 9$), and moves to the left, faster at early times and then becoming continuously slower. Secondly, as the cocoon pressure drops, the cocoon distribution of Fig. 27 moves towards the left (and somewhat down due to the mostly constant distribution in β at late times), and grows with cocoon volume too.

3.7 The lightest jets

The lightest jet in the series, M4, shows a very different behaviour from the other runs due to its strong magnetic fields, thus a run with lower magnetic fields (M4L) was performed in addition. In this section, we focus on the specific properties of and differences between these two runs.

Both simulations show unstable beams, which are temporally stopped, deflected or disrupted. This is quite natural for the very light jets, where the impact of cocoon vortices hitting the beam is stronger, when the beam shows lower inertia but the cocoon gas is

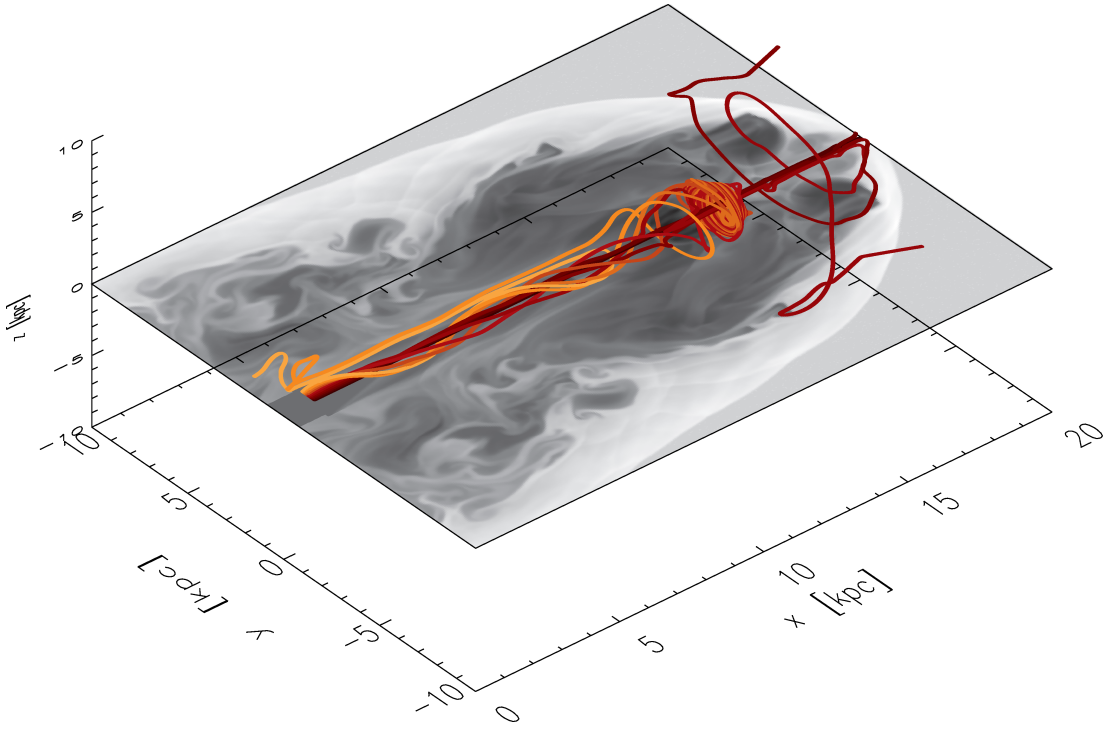

Figure 26. 3D magnetic field lines from within the beam with a transparent grey-scale logarithmic density slice in a plane through the jet axis. Model M2 at $t = 1.3$ Myr.

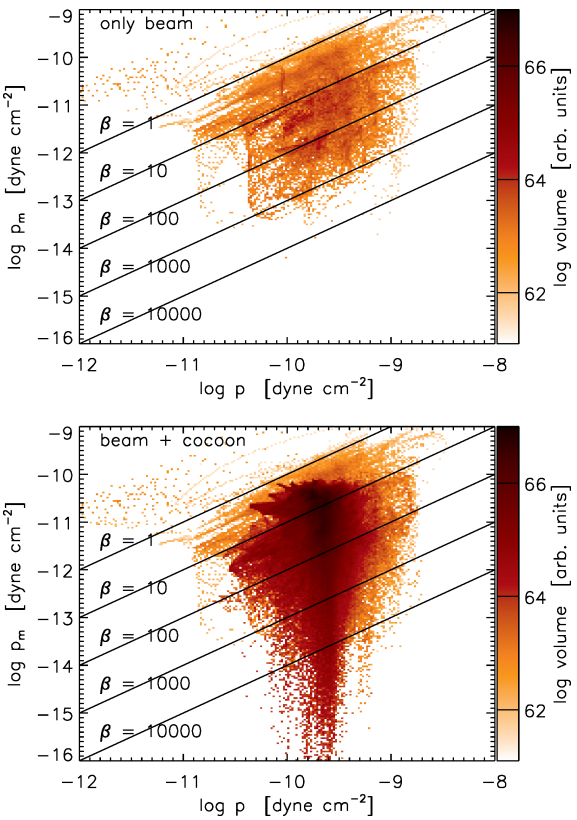

Figure 27. $p_{\rm m} - p$ histogram for the beam (defined by kinetic energy flux $\gtrsim$1 per cent of the maximum value) and all the jet matter from simulation M3 after 15 Myr. Lines of constant plasma β with values of 1, 10, 100, 1000 and 10 000 are overlaid.

dense due to entrainment and mixing with the dense ambient gas. This destabilization is particularly strong in axisymmetry, as the vortices cannot 'miss' the beam as they could in 3D. For M4L, after a strong deflection of the right beam near the nozzle ($t \approx 20$ Myr), a small region with strong poloidal field piles up just next to the nozzle and creates a magnetic layer ($\beta \gtrsim 1$) at the beam boundary. This protects the beam from cocoon vortices and entrainment, and from there on inhibits disruptions of the right jet, which then propagates more quickly than the left jet. At the end of the simulation, the right jet is ≈20 per cent longer than the left jet and shows an almost undisturbed beam up to the jet head. More detailed examination of this phenomenon may be interesting, but as it was only introduced by chance, the details are difficult to reproduce and beyond the scope of this paper. None the less, the overall propagation of the jet within the simulated time (Section 3.3.3) is not much affected by this.

Keeping the jet speed and the Mach number fixed, the ratio of the thermal pressures of ambient gas and jet nozzle changes with density contrast, yielding an underpressured jet for M4 and M4L. For M4, the magnetic field in the nozzle is already stronger than equipartition and the Alfvén speed is higher than the sound speed. This run is dynamically dominated by the magnetic field and shows a pronounced nose cone, which is known for jets with strong toroidal fields (Clarke et al. 1986). Magnetic tension pinches the jet matter into an narrow tube of 2.5–3.5 kpc radius, completely suppressing a backflow and thus preventing the formation of a wide cocoon. The simple case of a plasma column in radial magnetostatic equilibrium keeps $p + B_\phi^2/4\pi$ constant. If $B_\phi^2/4\pi$ approaches the thermal pressure, the magnetic pinch becomes important. In our case, the toroidal field in the plasma column is relatively homogeneous, showing a (volume-weighted) distribution mostly between 30 and 50 μG, while the thermal pressure lies (radially decreasing) in the

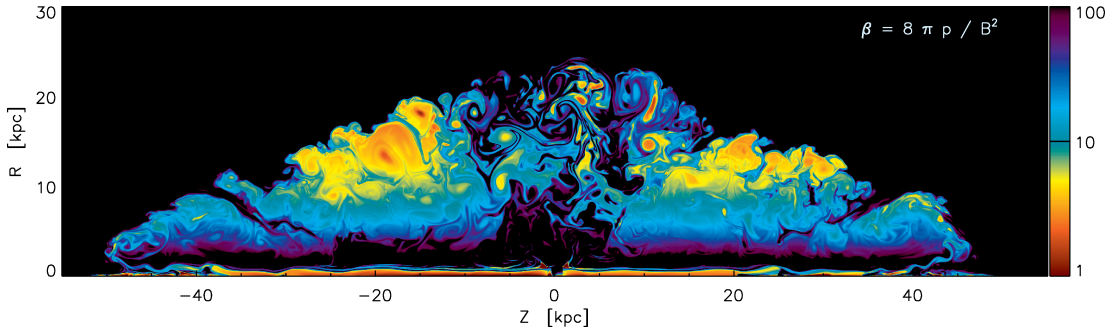

Figure 28. Plasma β distribution for M3 at 15 Myr, in logarithmic scaling.

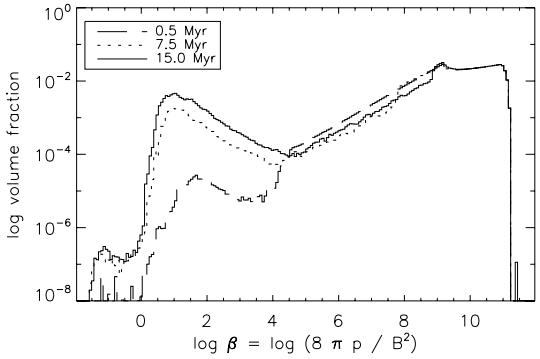

Figure 29. Volume-weighted histogram of plasma β for M3 at 0.5, 7.5 and 15 Myr.

range 1–3 $\times 10^{-10}$ dyne cm^{-2}, thus matching $p \sim B_\phi^2/4\pi$ and being just around equipartition. These values are not the ones set by the jet nozzle, although those that obey $p \sim B_\phi^2/4\pi$ too. The twisting and shearing processes described in the previous subsection are very strong due to the equipartition-level magnetic fields, the rotation around the jet axis can make up a large fraction of the total velocity, and the toroidal field component grows to the measured values.

Krause & Camenzind (2001) examined the convergence of a nose cone simulation and found that the Mach disc retreated towards the nozzle and thus did not converge. Also in M4, the Mach disc is very near to the jet nozzle, and the velocities after that shock are subsonic (although the nose cone itself propagates faster than the jet head in M4L). Thus, it is unclear, how reliable the run is. We also note that the magnetic pinch is subject to MHD instabilities (Clarke 1993), which might produce blobs and disrupt the plasma column in 3D. However, as this nose cone is produced by the magnetic tension of the strong toroidal field, this is not applicable to strong poloidal fields, which cannot provide the necessary hoop stress, although it seems difficult to maintain a strong poloidal field along an interacting beam without converting part of it into toroidal field, which then might again pinch the plasma.

4 DISCUSSION

4.1 Magnetic fields

Effects of magnetic fields naturally depend on their strength. Trying to understand the smoothness of jet cocoons in galaxy clusters, we concentrated on magnetic fields in jets which are not dominant, but still have significant effects on the jet dynamics, the best example for this being the M3 run with average plasma $\beta = 8$. It is well known (Miura & Pritchett 1982) that magnetic tension can damp or suppress KH instabilities and hence it may be the key to stabilizing the contact discontinuity between jet and ambient gas. However, how this applies to the complex case of jet–ambient interaction is not yet known.

We emphasize that much care was taken to use a globally consistent setup for our very light jets, in particular: keeping the bow shock inside the computational domain at all times; simulating bipolar (back-to-back) jets to remove an artificial boundary condition in the mid-plane and allow interaction of the backflows for a realistic lateral expansion and using a configuration which confines the magnetic field to the jet and has closed field lines instead of a homogeneous magnetic field reaching to infinity, which is then effectively anchored in the ambient gas. The assumed simplifications, axisymmetry and a constant ambient density make extraction of the underlying physics easier and effects of relaxing those for HD jets were previously investigated by Krause (2005). Thus, we expect to at least qualitatively model the situation realistically.

Two main effects arise from the inclusion of magnetic fields. First, in the jet head, we see that the provided magnetic fields in the jet do indeed stabilize the contact surface, which produces a pronounced jet head and lobes, similar to the ones seen in Cygnus A (Carilli et al. 1991) and other classical double radio sources. Effects from an ambient density profile can be excluded due to the prescribed constant density atmosphere. Furthermore, the entrainment of ambient gas is significantly smaller there than without magnetic fields.

Secondly, jets prove to be efficient generators of magnetic energy, transferring part of their huge kinetic power to magnetic fields through shearing in the jet head. This relies on some rotation of the beam plasma, which will (as seen in the simulations) generally be present for a non-zero toroidal field component. Some toroidal field is expected if the mostly axial field in the beam (Bridle & Perley 1984) is perturbed three-dimensionally and from jet formation models, where the toroidal field is necessary for jet collimation at least at small scales. The shearing mechanism provides a source of magnetic energy for the cocoon and furthermore affects the magnetic field structure at the hotspots and possibly some internal shocks. A radial and toroidal field component in the beam is known to be compressed by the terminal shock and is then visible as a strong magnetic field perpendicular to the jet axis. The jet head shearing provides another mechanism, independent from compression, to greatly enhance the toroidal field and thus produce a perpendicular field component stronger than that expected from compression. For jets pointing more towards the observer, the toroidal field around the hotspot region may become observable.

This may be relevant for several observational findings, one being the smoothness of radio cocoons. We have shown that even if the plasma β is of order 10, only, the fields in the backflow and the

cocoon, respectively, will be strong enough to damp KH instabilities at the cocoon–ambient gas interface and yield a morphology much smoother than seen in HD simulations, reconciling simulations with observations of sources as Cygnus A (Lazio et al. 2006), Pictor A (Perley et al. 1997) or Hercules A (Gizani & Leahy 2003), where the latter seems to be a past high-power source. Due to the 2.5D nature of the simulations, the effect is restricted to the jet head region. In a full 3D simulation, we expect therefore the cocoon–ambient interface to be more stable even further back from the hotspots. The amplification of beam magnetic fields in the 'jet head machine' furthermore is consistent with the observation of magnetic fields in the cocoon just somewhat below equipartition (Hardcastle & Croston 2005; Migliori et al. 2007). Additionally, the magnetic field predominantly perpendicular to the jet axis in weak FR I sources might be related to the expansion of the jet, which by the shearing would create strong toroidal fields in the absence of strong turbulence. Even though the beam rotation can change much due to interaction with the cocoon and shocks and even change sign, the helicity of the toroidal field is not changed and can thus link the field at large scales with the field topology near the black hole (Gabuzda et al. 2008).

For the magnetic field topology in the rest of the cocoon, axisymmetry is a major limitation, contrary to the effects discussed before. Magnetic field in a toroidal configuration cannot damp KH instabilities in axisymmetry since no magnetic tension is available as restoring force, while poloidal field could do so. Fortunately, the jet head-generated toroidal field in the turbulent cocoon partly would be converted into poloidal field in three dimensions, establishing some dynamical equilibrium between the components but keeping the overall field magnitude or amplify it even further, and this makes the cocoon magnetic field a reasonable explanation for the smooth contact surfaces. As a future step, we will examine this effect in three dimensions to be able to quantify the amount of damping and suppressed entrainment of ambient gas in the cocoon.

However, despite the inability to actually produce the expected smooth contact surfaces in axisymmetry away from the jet head region, there is no reason to assume that the amplification of magnetic fields should be in three dimensions any different than shown in our simulations, as the plasma dynamics are not very different and the shearing mechanism in the jet head simply relies on the off-axis flow of plasma, which also happens in 3D. Furthermore, we are not aware of any reason that the field magnitude in the cocoon should be much different in 3D. It is unclear, though, how the spatial distribution of the magnetic field would look like: 3D turbulence might want to distribute field strength rather uniformly in the cocoon, but formation of a large-scale poloidal current may try to establish a radially increasing toroidal field. Observations indicate that magnetic field strengths within the cocoon may vary considerably (Goodger et al. 2008).

It may be interesting to note that the amplification of magnetic field is quite related to dynamo action as in the sun. The shearing (Ω effect) is just the same and solar convection is replaced by jet-driven cocoon turbulence, but the location of these actions is different and they are externally powered (by the beam thrust) instead of self-sustained. The spatial separation of the two effects and the (at least roughly) isotropic turbulence, however, prevent the formation of an outstanding large-scale poloidal field.

The uncertainty in the magnetic field topology in the cocoon also applies to the distribution of plasma β in the system. We (expectedly) found that plasma β is unchanged throughout shocks despite a gradual increase along the beam (which might also be due to limited resolution of the beam and entrainment). Thus, the assumption of a fixed fraction of equipartition to generate synchrotron emission maps from hydro simulations seems to be quite justified. However, this was not found to be true for the cocoon, where a wide distribution of β was found and deriving synchrotron emission from hydro models thus may be far away from MHD results. But as mentioned, this result is expected to change in 3D, apart from having relatively low β in the cocoon. Emission maps of our simulations and comparison to hydro models are beyond the scope of this work and will be presented in a subsequent paper.

The amplification of magnetic fields is also particularly interesting for the question of the origin of lobe magnetic fields. De Young (2002) pointed out that equipartition fields in the lobes cannot be passively advected with the plasma from the jet beam due to flux conservation arguments. The beam magnetic fields would have to be of order 0.01 G or higher, certainly above equipartition, which would result in enormous synchrotron losses, luminosities incompatible with observational limits and probable disruption of the jet due to the magnetic pressure. Hence, the magnetic field must be amplified by some mechanism, and De Young argues for turbulent amplification in the hotspot flow, though it is not easy to meet the necessary requirements for this. The shearing in the jet head, which is seen in our simulations, in contrast, almost inevitably provides this amplification and can therefore explain the strong lobe magnetic fields or at least contribute to their field strength. In fact, the simulations exhibit field magnitudes in the cocoon that are comparable to field magnitudes in the beam and consequently have similar plasma β since the beam and cocoon pressures came to balance. We conclude that shearing due to off-axis flow of the plasma provides a natural explanation for the lobe magnetic fields and allows equipartition jets to inflate an equipartition cocoon.

4.2 Dynamical evolution

X-ray observations of the ambient cluster gas contain valuable information about several jet and AGN properties and self-similar models can give easy access to underlying physical parameters. In this paper, we are able to confirm agreement of our numerical simulations with self-similar models (Falle 1991; Begelman 1996; Kaiser & Alexander 1997; Komissarov & Falle 1998) for the bow shock propagation. Eccentricity of the bow shock and its Mach number seem to be an easy way to compare theoretical models with observations, without the need for uncertain assumptions on the emission of the radio plasma.

The weak and roundish bow shocks in observations indicate that models of very light jets (with density ratios $<10^{-2}$) are necessary for most cluster sources. Although we chose a simplified setup with a constant ambient gas and axisymmetry, the simulations are in the regime of observed values for various sources and self-similar models generalize this behaviour for declining cluster profiles, which was already examined for very light HD jets by Krause (2005). As our runs, with the clear exception of the magnetically dominated M4, propagate as their hydro counterparts, only minor deviations from those results are expected, except where specific source properties are to be included.

Contrary to the bow shocks and the jet length, we find that the cocoon width in general does not evolve self-similarly but for lighter jets grows with lower power-law exponents and the mean cocoon pressure drops more slowly than expected. Although this may seem unexpected, it was already stated by Kaiser & Alexander (1997) that contrary to the bow shock the self-similar evolution of the cocoon depends on the physical model for the post-hotspot flow and thus deviations are to be expected if these assumption do not

hold in the simulations. Since very light jet cocoons are less overpressured and approach the ambient pressure sooner, the sideways expansion becomes slower and may even stall, letting their aspect ratio (length-to-width ratio) grow. This is in fact observed by Mullin et al. (2008), who find a wider range of aspect ratios, once the source size approaches ∼100 kpc. Similar behaviour would be expected for the heavy jets, although at much later times. Thus, cocoon evolution depends sensitively on the question of overpressure, which can be addressed by the strength of the lateral bow shock. Self-similar models, in contrast, assume that the ambient pressure is negligible. Komissarov & Falle (1998) defined two scales, l_c and L_c, between which they found self-similar evolution. The lower bound l_c, where the swept-up mass equals the jet mass, is much smaller than the jet radius in our simulations, and the upper bound L_c, where the ambient pressure becomes important, is comparable to our computational domain size. Accordingly, while they observe the self-similarity being established, we observe its end, explaining why our less overpressured numerical solutions gradually deviate from a self-similar evolution.

Furthermore, cluster density profiles make cylindrical cocoons rather than elliptical ones due to the weaker density contrast at larger distances (Krause 2005). Altogether, this makes us confident that our simulations reasonably well describe observed cluster sources.

In contrast to bow shocks, measurements of the cocoon shape are complicated by cooling of the relativistic electrons, which limits observations to the outermost parts (lobes). While radio observations show the high-energy electrons in the cocoon as lobes, single-fluid MHD simulations only trace the low-frequency emitting matter and can only show the low-frequency radio morphologies (cf. high- and low-frequency images in Carilli et al. 1991), which generally suffer from low spatial resolution. This situation fortunately will much improve in the future with new telescopes as LOFAR or the SKA, which will allow more detailed studies of cocoon dynamics and turbulence. Until then, X-ray images of cavities and (in some cases) the inverse-Compton emission off the cosmic microwave background may supplement available low-frequency radio maps.

Scheuer (1982) introduced the 'dentist's drill' to refer to a moving working surface, which therefore widens the jet head and the lobes. Very light jets naturally show extensive cocoons and varying deflection of the beam widens the jet head and hence, even in axisymmetry, show something very similar to a 'dentist's drill'. While this does not exclude beam precession (Steenbrugge & Blundell 2008), it is does not require it and no large precession amplitudes are needed a priori.

We expect for multiple outbursts of different power in the same cluster, indicated by 'ghost cavities' (e.g. Fabian et al. 2006; Wise et al. 2007), that their evolution crucially depends on the history of the past outbursts, as these push the dense cluster gas aside, letting the new outburst propagate with different density contrast. In this case, the new jet might quickly push forward to the old jet size, then resuming its work on the dense ambient gas. The morphology of the cavities may allow the determination of the respective density contrasts and thus could shed light on the outburst history.

The thermal interaction of jets with the intracluster medium is less accessible to direct comparison with observations. Slower jet head propagation is responsible for the strong impact of the beam at the working surface and a high thermalization; some conversion of kinetic to thermal energy will additionally occur near or in the beam due to beam destabilization, but may be less effective in 3D. Despite the dominant power source is the kinetic jet power, this strong thermalization converts most of the input power to thermal energy – about half of this in the shocked ambient gas and half in a cocoon filled with high-entropy plasma, which eventually may transfer at least part of its energy to the entrained cluster gas. This is in line with findings of other authors (e.g. Reynolds et al. 2002; O'Neill et al. 2005; Zanni et al. 2005), where the latter authors conclude that up to 75 per cent of the energy can be dissipated irreversibly and thus is available for heating in the intracluster medium, as required by the X-ray luminosity–temperature relation (Magliocchetti & Brüggen 2007) and to provide 'radio-mode' feedback for models of galaxy evolution (Croton et al. 2006).

Since only the hot gas phase is simulated, effects on the cold or warm phases of the interstellar medium (ISM) of galaxies are difficult to estimate. Clearly, the thermalization efficiency cannot be simply applied to the cold gas. Simulations of multiphase turbulence in the jet cocoon by Krause & Alexander (2007) with their higher spatial resolution can resolve the different phases and provide a complementary view (microphysics) on to the jet–cloud interaction. However, even if the thermal energy mostly is deposited on the hot gas phase (at larger distances), it is evident from our simulations that the jet cocoon is a rich reservoir of turbulent kinetic energy which will act on the cold gas phase of the galaxy over a time-scale corresponding to the decay time-scale of the cocoon turbulence. For a jet of power 10^{46} erg s^{-1} being active for 10^7 years, the turbulent energy stored in the cocoon is expected to be of the order of a few $\times 10^{59}$ erg and over a time possibly longer than the jet activity will interact with the cold ISM phases.

Another interesting result of the present simulations is the excitation of sound waves in the ambient gas by vortices in the turbulent cocoon, which is more effective for the very light jets with their extended cocoons. Vortex shedding (Norman et al. 1982) quasi-periodically occurs in the jet head, and the vortices then are advected with the backflow into the cocoon and provide an intermittent source for the turbulent cascade, producing pressure waves. Waves like these are visible in the Perseus cluster (Fabian et al. 2006; Shabala & Alexander 2007) and, although being hard to observe, may be an ubiquitous feature in galaxy clusters with current or past jet activity. Their typical wavelength might yield a link to jet dynamics and cocoon turbulence. In the lightest of our jets (M4L), the bow shock is just about to turn into a sound wave and then simply would join the enclosed sound waves. Viscous damping may be a mechanism to reduce the amplitudes in addition to the growing wave area and is another candidate for preventing cooling flows (Fabian et al. 2005), but in our scenario would be related to the jets rather than to the AGN itself.

Axisymmetry naturally imposes some constraints on the dynamics, which have to be considered carefully. Jet beams in high-power sources are essentially axisymmetric objects and effects of the full third dimension are merely perturbations from axisymmetry. However, this obviously is not true when beam stability or non-axisymmetric effects are explored specifically. While generally 3D jets are subject to a greater number of instabilities, for very light jets there is an opposing effect of an increased number of dimensions. While in 3D, cocoon vortices often will miss the beam or are slightly deflected, this is not possible in axisymmetry and the beam thus is destabilized, deflected or disrupted more easily which is most evident from our lightest run (M4L). As seen in the very light jets of Krause (2005), the beam stability improves when going to full three dimensions. For most results, however, energetics and scaling behaviour are not expected to change significantly in 3D, notable exceptions to this being cocoon turbulence, magnetic field topology and stability of the contact discontinuity.

Cocoon turbulence further away from the jet head certainly will differ with increased dimensionality as the increased number of

degrees of freedom for vortices allows them to turn in all directions and interactions between colliding vortices will be different. Though, we expect the effects on cocoon morphology to be within reasonable limits, as the kinetic energy in the cocoon is lower than the thermal energy by factors of $\gtrsim 3$ for $\eta \leq 10^{-2}$ and hence effects of thermal pressure will dominate.

5 CONCLUSIONS AND SUMMARY

We performed a series of axisymmetric hydrodynamic and magnetohydrodynamic simulations of bipolar very underdense jets in a constant density atmosphere. The magnetic field is mostly confined to the jet with a helical topology.

(1) We find that the magnetic fields damp Kelvin–Helmholtz instabilities in the jet head and stabilize it. They produce smoother and more pronounced outer lobes already with a plasma $\beta \sim 10$. The entrainment of ambient gas into the cocoon is considerably suppressed there. This morphology is more consistent with observations of powerful double radio sources than are hydrodynamic simulations, which show a ragged cocoon boundary.

(2) Magnetic fields are efficiently amplified in the jet head by shearing as the plasma streams off the jet axis. This originates from a rotation of the beam which we find to be a general result of a toroidal field component being present (yet not necessarily dominant) in the jet. The shearing converts part of the huge kinetic energy into magnetic energy and provides the cocoon with a magnetic field much stronger than expected from flux conservation, in some regions even approaching equipartition. These findings are consisistent with recent observations of near-equipartition magnetic fields in cocoons derived from radio/inverse-Compton emission observations. Already in our axisymmetric simulations the fields are in principle strong enough to stabilize the contact surface between the cocoon and the ambient gas all over the cocoon and not only in the jet head. The necessary change in field topology would be a consequence expected of fully 3D turbulence in the cocoon.

(3) The amplified magnetic field is mostly toroidal, resulting in a stronger contribution of the field component perpendicular to the jet axis than expected from pure compression of magnetic fields at the hotspots. It is also expected at locations where a jet widens considerably (as in FR I sources). In the backflow and the cocoon, however, turbulence will probably establish some balance between the magnetic field components, which could not be established in axisymmetry.

(4) The very light jets show round bow shocks with low Mach numbers. We find that the bow shocks evolve self-similarly and hence give a simple link between observations and some underlying physical parameters. The cocoon width, however, evolves self-similarly only for jets in their highly overpressured phases, but grows slower as the cocoons approach pressure balance with the ambient gas and the bow shock Mach number drops. These sources thus are surrounded by thick layers of shocked ambient gas.

(5) The jet cocoon shows highly turbulent motion. It is driven by vortices shed in the jet head, which are advected with the backflow. Interaction of these vortices with the ambient gas excites waves and ripples in the shocked ambient gas, which are joined by the dissolving bow shock at later stages.

(6) The strong thermalization that occurs for very light jets transfers most of the jet power to the thermal energy of the cocoon and the shocked ambient gas, making it available for heating of the cluster gas and radio-mode feedback. In addition to this, the turbulent motion in the cocoon is associated with a considerable amount of kinetic energy ($\sim$10 per cent of the jet power) that may provide efficient feedback on to the cold phase of the galaxy's ISM.

ACKNOWLEDGMENTS

We thank Paul Alexander and Martin Hardcastle for helpful discussions as well as the anonymous referee for suggestions that further improved this paper. This work was supported by the Deutsche Forschungsgemeinschaft (Sonderforschungsbereich 439). The simulations partly have been carried out on the NEC SX-6 of the HLRS Stuttgart (Germany).

REFERENCES

Alexander P., Leahy J. P., 1987, MNRAS, 225, 1
Aloy M. A., Ibáñez J. M., Martí J. M., Gómez J.-L., Müller E., 1999, ApJ, 523, L125
Balsara D. S., Norman M. L., 1992, ApJ, 393, 631
Begelman M. C., 1996, in Carilli C. L., Harris D. E., eds, Cygnus A – Study of a Radio Galaxy. Cambridge Univ. Press, Cambridge, p. 209
Blandford R., 2008, in Rector T. A., De Young D. S., eds, ASP Conf. Ser. Vol. 386, Extragalactic Jets: Theory and Observation from Radio to Gamma Ray. Astron. Soc. Pac., San Francisco, p. 3
Bridle A. H., 1982, in Heeschen D. S., Wade C. M., eds, Extragalactic Radio Sources, IAU Symp. 97. Reidel, Dordrecht, p. 121
Bridle A. H., Perley R. A., 1984, ARA&A, 22, 319
Cabral B., Leedom L. C., 1993, in SIGGRAPH '93: Proc. 20th Annu. Conf. Computer Graphics and Interactive Techniques. ACM, New York, p. 263
Camenzind M., 1990, in Klare G., ed., Rev. Mod. Astron., 3, 234
Carilli C. L., Perley R. A., Dreher J. W., Leahy J. P., 1991, ApJ, 383, 554
Carvalho J. C., O'Dea C. P., 2002a, ApJS, 141, 337
Carvalho J. C., O'Dea C. P., 2002b, ApJS, 141, 371
Clarke D. A., 1993, in Röser H. J., Meisenheimer K., eds, Jets in Extragalactic Radio Sources, Lecture Notes in Phys. Vol. 421. Springer, Berlin, p. 243
Clarke D. A., Norman M. L., Burns J. O., 1986, ApJ, 311, L63
Clarke D. A., Harris D. E., Carilli C. L., 1997, MNRAS, 284, 981
Croston J. H., Hardcastle M. J., Harris D. E., Belsole E., Birkinshaw M., Worrall D. M., 2005, ApJ, 626, 733
Croton D. J. et al., 2006, MNRAS, 365, 11
De Young D. S., 2002, New Astron. Rev., 46, 393
Fabian A. C., Reynolds C. S., Taylor G. B., Dunn R. J. H., 2005, MNRAS, 363, 891
Fabian A. C., Sanders J. S., Taylor G. B., Allen S. W., Crawford C. S., Johnstone R. M., Iwasawa K., 2006, MNRAS, 366, 417
Falle S. A. E. G., 1991, MNRAS, 250, 581
Fanaroff B. L., Riley J. M., 1974, MNRAS, 167, 31
Gabuzda D. C., Vitrishchak V. M., Mahmud M., O'Sullivan S. P., 2008, MNRAS, 384, 1003
Gaibler V., Vigelius M., Krause M., Camenzind M., 2006, in Nagel W. E., Jäger W., Resch M., eds, High Performance Computing in Science and Engineering. Springer-Verlag, Berlin, p. 35
Gizani N. A. B., Leahy J. P., 2003, MNRAS, 342, 399
Goodger J. L., Hardcastle M. J., Croston J. H., Kassim N. E., Perley R. A., 2008, MNRAS, 386, 337
Hardcastle M. J., Croston J. H., 2005, MNRAS, 363, 649
Hardee P. E., 2000, ApJ, 533, 176
Hardee P. E., Clarke D. A., 1995, ApJ, 451, L25
Heinz S., Brüggen M., Young A., Levesque E., 2006, MNRAS, 373, L65
Kaiser C. R., Alexander P., 1997, MNRAS, 286, 215
Keppens R., Meliani Z., van der Holst B., Casse F., 2008, A&A, 486, 663
Komissarov S. S., 1999, MNRAS, 308, 1069
Komissarov S. S., Falle S. A. E. G., 1998, MNRAS, 297, 1087
Kössl D., Müller E., Hillebrandt W., 1990, A&A, 229, 378
Krause M., 2003, A&A, 398, 113
Krause M., 2005, A&A, 431, 45

Krause M., Alexander P., 2007, MNRAS, 376, 465
Krause M., Camenzind M., 2001, A&A, 380, 789
Lazio T. J. W., Cohen A. S., Kassim N. E., Perley R. A., Erickson W. C., Carilli C. L., Crane P. C., 2006, ApJ, 642, L33
Leismann T., Antón L., Aloy M. A., Müller E., Martí J. M., Miralles J. A., Ibáñez J. M., 2005, A&A, 436, 503
Li H., Lapenta G., Finn J. M., Li S., Colgate S. A., 2006, ApJ, 643, 92
Lind K. R., Payne D. G., Meier D. L., Blandford R. D., 1989, ApJ, 344, 89
McNamara B. R., Nulsen P. E. J., 2007, ARA&A, 45, 117
McNamara B. R., Nulsen P. E. J., Wise M. W., Rafferty D. A., Carilli C., Sarazin C. L., Blanton E. L., 2005, Nat, 433, 45
Magliocchetti M., Brüggen M., 2007, MNRAS, 379, 260
Meisenheimer K., Röser H. J., Hiltner P. R., Yates M. G., Longair M. S., Chini R., Perley R. A., 1989, A&A, 219, 63
Migliori G., Grandi P., Palumbo G. G. C., Brunetti G., Stanghellini C., 2007, ApJ, 668, 203
Miley G., De Breuck C., 2008, A&Ar, 15, 67
Miura A., Pritchett P. L., 1982, J. Geophys. Res., 87, 7431
Mizuno Y., Hardee P., Nishikawa K. I., 2007, ApJ, 662, 835
Mullin L. M., Riley J. M., Hardcastle M. J., 2008, MNRAS, 390, 595
Norman M. L., Winkler K. H. A., Smarr L., Smith M. D., 1982, A&A, 113, 285
O'Neill S. M., Tregillis I. L., Jones T. W., Ryu D., 2005, ApJ, 633, 717
Perley R. A., Röser H. J., Meisenheimer K., 1997, A&A, 328, 12
Reynolds C. S., Heinz S., Begelman M. C., 2002, MNRAS, 332, 271
Rosen A., Hughes P. A., Duncan G. C., Hardee P. E., 1999, ApJ, 516, 729
Saxton C. J., Bicknell G. V., Sutherland R. S., 2002a, ApJ, 579, 176
Saxton C. J., Sutherland R. S., Bicknell G. V., Blanchet G. F., Wagner S. J., 2002b, A&A, 393, 765
Scheuer P. A. G., 1982, in Heeschen D. S., Wade C. M., eds, Extragalactic Radio Sources, IAU Symp. 97. Reidel, Dordrecht, p. 163
Shabala S., Alexander P., 2007, Ap&SS, 311, 311
Smith D. A., Wilson A. S., Arnaud K. A., Terashima Y., Young A. J., 2002, ApJ, 565, 195
Steenbrugge K. C., Blundell K. M., 2008, MNRAS, 388, 1457
Sutherland R. S., Bicknell G. V., 2007, ApJS, 173, 37
Tregillis I. L., Jones T. W., Ryu D., 2001, ApJ, 557, 475
Tregillis I. L., Jones T. W., Ryu D., 2004, ApJ, 601, 778
Wise M. W., McNamara B. R., Nulsen P. E. J., Houck J. C., David L. P., 2007, ApJ, 659, 1153
Zanni C., Bodo G., Rossi P., Massaglia S., Durbala A., Ferrari A., 2003, A&A, 402, 949
Zanni C., Murante G., Bodo G., Massaglia S., Rossi P., Ferrari A., 2005, A&A, 429, 399
Ziegler U., Yorke H. W., 1997, Comput. Phys. Communications, 101, 54

This paper has been typeset from a TEX/LATEX file prepared by the author.